GEO 610: Master's Thesis

Retrieval of higher order statistical moments from full-waveform LiDAR data for tree species classification

Remote Sensing Laboratories
Department of Geography
University of Zurich
Winterthurerstrasse 190
CH-8057 Zurich
Switzerland

Master Thesis	July 31, 2016
Author:	Moritz Bruggisser
Matriculation-Nr:	10-101-152
E-Mail:	moritz.bruggisser@gmail.com
Phone:	+41 79 512 54 24
Faculty Representative:	Prof. Dr. Michael E. Schaepman
Supervisor:	Dr. Felix Morsdorf

Abstract

Airborne laser scanning (ALS) offers the unique opportunity to quantitatively assess three-dimensional forest structure over large areas and, thus, to provide important information for tree inventories. Tree inventories, inter alia, need information on the tree species. Previous studies aimed at distinguishing tree species based on three-dimensional tree structure metrics derived from the ALS point cloud or based on features from full-waveform (FW) laser scanning data provided by today's sensors. Classifications based on FW features mainly use echo amplitude, energy and width, which are typically retrieved by waveform decomposition, often performed using the symmetric Gaussian distribution function.

However, for forested areas, the symmetry of the echo shape is potentially modified by multiple scattering and the distribution of scattering elements (e.g. leafs). In this study, we assess the potential of processing full-waveform ALS data such that the third and fourth statistical moments, i.e. the echo skewness and the echo kurtosis, can be retrieved additionally. For this purpose, we propose a waveform decomposition using the skew normal distribution function (SND), which enables the modelling of skewed echoes. We subsequently investigate the differences of tree-crown aggregated SND derived FW features between seven tree species within a temperate mixed forest with the aim of detecting the most descriptive echo features. Eventually, the derived FW features are tested for a species classification.

The results reveal that the largest differences across the tree species are in the mean energy of the first echoes (15 out of 21 species pairs show differences), followed by the mean amplitude of the first echoes and the mean skewness of all echoes originating from a single crown (14 out of 21 species pairs show differences against each other for both features).

The differentiation of coniferous and deciduous trees benefits from the features derived from the SND decomposition compared to the use of echo amplitude only (0.39 vs. 0.61 in Cohen's κ). As the classification power of the three dominant tree species within the test site shows mediocre increase (0.20 vs. 0.25 in Cohen's κ), we propose the use of the derived features in combination with features from multispectral data for this purpose. We attribute the difficulties in the tree species classification to the relatively wide ranges of the crown aggregated features within one species, which for some features results in a considerable overlap of the feature ranges across the species.

The SND decomposition is comparable to the Gaussian decomposition regarding the decomposition accuracy ($RMSE = 5.08$ vs. $RMSE = 4.05$) and computational cost.

Hence, we propose the default use of the SND decomposition, as the SND is a more flexible function, allowing for the modelling of normally distributed echoes, as well as the fitting of skewed echoes, while no limitations regarding the direction of the skewness are introduced.

Zusammenfassung

Flugzeuggestütztes Laserscanning (engl. ALS) bietet einzigartige Möglichkeiten zur quantitativen Erfassung der dreidimensionalen Waldstruktur über grosse Flächen hinweg und kann damit wichtige Informationen für Bauminventare liefern. Bauminventare beinhalten unter anderem die Information über die Baumarten. Bisherige Studien zielten darauf, die Baumarten entweder basierend auf Metriken der dreidimensionalen Baumstruktur zu unterscheiden, welche aus ALS-Punktwolken extrahiert wurden, oder basierend auf Full-Waveform (FW) Laserscanning Daten, welche von heutigen Sensoren geliefert werden. Klassifikationen basierend auf FW-Merkmalen nutzen vorwiegend die Amplitude, die Energie und die Breite des Echos, wie sie typischerweise durch eine Waveform-Zerlegung erhalten werden. Für diese Zerlegung wird meist die symmetrische Gauss-Verteilung verwendet.

Für bewaldete Flächen wird die Echoform jedoch möglicherweise durch Mehrfachstreuung sowie durch die Verteilung der Streuelemente (z. B. Blätter) verändert. In dieser Studie untersuchen wir die Möglichkeit, die Full-Waveform ALS-Daten in einer Weise zu prozessieren, dass zusätzlich das dritte und vierte statistische Moment, d.h. die Echoschiefe und die Echowölbung, berechnet werden können. Zu diesem Zweck schlagen wir eine Waveform-Zerlegung unter Verwendung der Schiefen Normalverteilung (engl. SND) vor, welche die Modellierung von schiefen Echos ermöglicht. Anschliessend untersuchen wir die Unterschiede der SND-basierten und innerhalb der Baumkrone aggregierten FW-Merkmale zwischen sieben Baumarten eines gemässigten Mischwaldes. Das Ziel dabei ist es, die aussagekräftigsten Echomerkmale zu finden. Schliesslich werden die FW-Merkmale für die Verwendung in einer Baumartenklassifikation getestet.

Die Resultate zeigen, dass die grössten Unterschiede zwischen den Baumarten in der gemittelten Energie der Erst-Echos zu finden sind (15 von 21 Artenpaare zeigen Unterschiede), gefolgt von der gemittelten Amplitude der Erst-Echos und der gemittelten Schiefe aller Echos, welche einer einzelnen Baumkrone entstammen (14 von 21 Artenpaaren zeigen Unterschiede gegeneinander für diese beiden Merkmale).

Die Unterscheidung von Laub- und Nadelbäumen zeigt den Nutzen der Merkmale, wie sie von der SND-Zerlegung abgeleitet werden können, im Vergleich zur Verwendung ausschliesslich der Echo-Amplitude (0.39 gegenüber 0.61 gemessen als Cohen's κ). Die Güte der Klassifikation der drei dominierenden Baumarten des Testgebiets zeigt demgegenüber eine mässige Verbesserung (0.20 gegenüber 0.25 gemessen als Cohen's κ). Wir schlagen deshalb vor, für die Artenklassifikation die abgeleiteten Echo-Merkmale in Kombination

mit Merkmalen aus Multispektraldaten zu verwenden. Die Schwierigkeiten für die Baumartenklassifikation erklären wir uns durch die relativ weiten Wertebereiche der kronenaggregierten Merkmale innerhalb derselben Baumart, was für einige Merkmale zu einer beträchtlichen überlappung der Merkmalsbereiche über die Baumarten hinweg führt.

Die SND-Zerlegung ist hinsichtlich der Genauigkeit ($RMSE = 5.08$ gegenüber $RMSE = 4.05$) und hinsichtlich des Rechenaufwandes vergleichbar mit der Gaussschen Zerlegung. Wir schlagen deshalb die standardmässige Verwendung der SND-Zerlegung vor, da die Schiefe Normalverteilung eine flexiblere Funktion ist, welche das Modellieren von normalverteilten Echos ermöglicht, gleichzeitig aber auch jenes von schiefen Echos, während keine Einschränkungen hinsichtlich der Richtung der Schiefe eingeführt werden.

Table of Contents

List of Figures

List of Tables

List of Abbreviations

1D	One-dimensional
3D	Three-dimensional
ALS	Airborne Laser Scanning
ANOVA	Analysis of Variance
CHM	Canopy Height Model
DTM	Digital Terrain Model
FW	Full-Waveform
FWHM	Full Width at Half Maximum
ICP	Iterative Closest Point
ITC	Individual Tree Crown
LiDAR	Light Detection And Ranging
m.a.s.l.	Meters Above Sea Level
MTA	Multiple Times Around
OA	Overall Accuracy
PA	Producer's Accuracy
PAI	Plant Area Index
PRF	Pulse Repetition Frequency
RF	Random Forest
RFD	Relative Frequency Distribution
SBET	Smoothed Best Estimate of Trajectory
SND	Skew Normal Distribution
socs	Scanner's Own Coordinate System
SVM	Support Vector Machines
UA	Users's Accuracy
UAV	Unmanned Aerial Vehicle
UTM	Universal Transverse Mercator

1 | Introduction

Biodiversity on a global scale is subject to loss, mainly driven by habitat change, including the invasion of alien species, climate change, overexploitation and pollution. This also applies to forests. Forests are one of the most diverse ecosystems and provide a variety of ecosystem services and goods relevant for the well-being of humans (Millennium Ecosystem Assessment, 2005). Reliable information on the state of the forests are a prerequisite to facilitate a sustainable management assuring the conservation of their biodiversity (FAO, 2010). In this context, the distribution of tree species is one of the attributes aimed at gathering (Millennium Ecosystem Assessment, 2005).

Remote sensing techniques offer possibilities for the acquisition of relevant biodiversity measures on a large scale and on an operational basis at affordable costs. For the management of forests in particular, Airborne laser scanning (ALS) offers the advantage of directly providing structural information of the forest canopy. Furthermore, as today's full-waveform (FW) laser scanners provide a discretised approximation of the backscattered energy (Leiterer et al., 2015), additional information on the reflectivity of the objects in the respective wavelength of the laser can be retrieved.

However, processing of FW data is challenging. A first issue lies in the nature of FW data which does not provide a spatially explicit point cloud, but requires the detection of the returns within the waveform, followed by a thorough georeferencing step. A second issue relates to the large data volumes which have to be handled. This demands fully automated, computationally efficient algorithms in order to accomplish waveform processing. This stands in contrast to laser scanner systems which directly detect and store a limited number of echoes. Such multiple discrete returns systems have lower storage requirements and reduce the computation costs. On the other hand, if a waveform processing chain is established, FW data has the advantage to enable the retrieval of additional echo features which are not provided by multiple discrete returns systems (e.g. Wagner et al., 2006) and furthermore allows for the detection of overlapping echoes (Chauve et al., 2007).

FW features derived through signal analysis in combination with structural information can, for instance, be used for tree species classification (e.g. Reitberger et al., 2008; Heinzel & Koch, 2011; Hovi et al., 2016). For a proper classification, detailed descriptions of the objects on the ground are required. In previous classification frameworks based on ALS data, the amplitude (e.g. Ørka et al., 2009), the intensity (e.g. Reitberger et al., 2008), the echo width (e.g. Reitberger et al., 2008; Heinzel & Koch, 2011) or the backscatter cross section (Hollaus et al., 2009) have been used as FW features.

In this thesis, we investigate the potential to extract more advanced echo attributes which could enlarge the feature space describing the tree species. In particular, we aim at the analysis of the third and fourth statistical moments of the return echoes, i.e. the skewness and the kurtosis, respectively, based on waveform decomposition. Subsequently the differences between the tree species present in the echo features are investigated and their potential for the improvement of tree species classifications is assessed.

The findings are summarized in Chapter 2, which includes the first-authored journal article, which will be submitted to ”Remote Sensing of Environment”. In Chapter 3, the statement of the hypothesis underlying our approach is described in more detail. Furthermore, this chapter provides supplementary information on aspects of waveform processing, which could not be discussed in the article, namely the georeferencing and the implementation of the decomposition. Finally, in Chapter 4, the approach is embedded into the current research and the results are briefly reflected.

2 | Retrieval of higher order statistical moments from full-waveform LiDAR data for tree species classification

This chapter bases on:
Bruggisser, M., Roncat, A., Schaepman, M. E. & Morsdorf, F. (in preparation).
Retrieval of higher order statistical moments from full-waveform LiDAR data for tree species classification.
which will be submitted to:
Remote Sensing of Environment

Contribution:

Design	75%
Materials & Methods	80%
Results & Conclusions	80%

Abstract

Airborne laser scanning (ALS) offers the unique opportunity to quantitatively assess three- dimensional forest structure over large areas and, thus, to provide important information for tree inventories. Tree inventories, inter alia, need information on the tree species. Previous studies aimed at distinguishing tree species based on three-dimensional tree structure metrics derived from the ALS point cloud or based on features from full-waveform (FW) laser scanning data provided by today's sensors. Classifications based on FW features mainly use echo amplitude, energy and width, which are typically retrieved by waveform decomposition, often performed using the symmetric Gaussian distribution function.

However, for forested areas, the symmetry of the echo shape is potentially modified by multiple scattering and the distribution of scattering elements (e.g. leafs). In this study, we assess the potential of processing full-waveform ALS data such that the third and fourth statistical moments, i.e. the echo skewness and the echo kurtosis, can be retrieved additionally. For this purpose, we propose a waveform decomposition using the skew normal distribution function (SND), which enables the modelling of skewed echoes. We subsequently investigate the differences of tree-crown aggregated SND derived FW features between seven tree species within a temperate mixed forest with the aim of detecting the most descriptive echo features. Eventually, the derived FW features are tested for a species classification.

The results reveal that the largest differences across the tree species are in the mean energy of the first echoes (15 out of 21 species pairs show differences), followed by the mean amplitude of the first echoes and the mean skewness of all echoes originating from a single crown (14 out of 21 species pairs show differences against each other for both features).

The differentiation of coniferous and deciduous trees benefits from the features derived from the SND decomposition compared to the use of echo amplitude only (0.39 vs. 0.61 in Cohen's κ). As the classification power of the three dominant tree species within the test site shows mediocre increase (0.20 vs. 0.25 in Cohen's κ), we propose the use of the derived features in combination with features from multispectral data for this purpose. We attribute the difficulties in the tree species classification to the relatively wide ranges of the crown aggregated features within one species, which for some features results in a considerable overlap of the feature ranges across the species.

The SND decomposition is comparable to the Gaussian decomposition regarding the decomposition accuracy ($RMSE = 5.08$ vs. $RMSE = 4.05$) and computational cost. Hence, we propose the default use of the SND decomposition, as the SND is a more flexible function, allowing for the modelling of normally distributed echoes, as well as the fitting of skewed echoes, while no limitations regarding the direction of the skewness are introduced.

Keywords Airborne laser scanning, Small-footprint, Echo skewness, Skew Normal Distribution, Forest management

2.1 Introduction

Tree inventories traditionally comprise measures of the extent, volume, composition and condition of the trees and stands (Kangas et al., 2006; Hyyppä et al., 2008; Wulder et al., 2008), but also include the tree species (Hyyppä et al., 2008; Hollaus et al., 2009; Hovi et al., 2016). Tree species information is an important information, required for habitat quality assessments or to infer the susceptibility to loss of the stand, for instance (Vaughn et al., 2012).

However, ground-based field inventories are expensive, as they are labor-intensive and thus, most often are either constrained to small areas or to a sampling design (Torabzadeh et al., 2014; Vauhkonen et al., 2014). Remote sensing, on the other hand, offers the possibility to provide biophysical vegetation information for large areas (Koetz et al., 2006; Torabzadeh et al., 2014) and has a long tradition in ecosystem monitoring (Ustin et al., 2004; Lu, 2006; Malenovský et al., 2009; Schaepman et al., 2009). For the collection of forest inventory attributes related to the tree height and canopy density, respectively, airborne laser scanning (ALS) is of particular value for information acquisition, comprising both a three-dimensional and a one-dimensional information dimension. The advantage of ALS compared to optical remote sensing is its ability to penetrate the forest canopy providing detailed three-dimensional information on the structure of the forest (Nilsson, 1996; Nelson et al., 1997; Lefsky et al., 1999; Hyyppä et al., 2008). Many inventory parameters relevant for forest management can be extracted directly from the acquired ALS point cloud, whereby ALS using small-footprint laser scanners today are used at operational level (Naesset, 2002; Wulder et al., 2013; Næsset, 2014; Hovi et al., 2016).

As ALS remote sensing is an active measurement, where energy in form of a laser pulse is emitted, it is furthermore possible to measure the intensity of the backscattered echoes, which describes the geometric-optical properties of the scatterers at the particular wavelength of the laser. The intensity information of discrete targets was used in forestry applications before (Holmgren & Persson, 2004; Brandtberg, 2007; Morsdorf et al., 2010)

In today's full-waveform laser scanners, the returning energy is digitized as a function of range and recorded. The backscattered waveform, which can be considered as a one-dimensional information source, is a result of the convolution of the emitted laser pulse with the cross-sections of the targets within the footprint of the laser (Wagner et al., 2006). Hence, its shape is determined by the characteristics of the single scatterers, namely their illuminated area, their reflectance, their orientation regarding to the laser beam direction and their spatial arrangement (Wagner et al., 2006; Höfle & Pfeifer, 2007; Hovi & Korpela, 2014; Hovi et al., 2016). However, the interactions of the laser pulse with elements constituting the forest structure are complex (Romanczyk et al., 2013) and the influence of multiple scattering on the return waveform have been discussed, both for large-footprint systems (Blair & Hofton, 1999; Sun & Ranson, 2000; Ni-Meister et al., 2001) and for small-footprint systems (Morsdorf et al., 2009; Hovi & Korpela, 2014). On the other hand, the recorded waveform additionally depends on the shape of the transmitted waveform and the impulse response of the receiver (Jutzi & Stilla, 2006a), further altering the waveform shape.

The many factors affecting the recorded waveform make the interpretation of the 1D waveform data challenging (Hovi et al., 2016). Usually, waveform processing aims at fitting known distribution functions to the waveform, i.e. performing a waveform decomposition (Hofton et al., 2000; Wagner et al., 2006; Mallet & Bretar, 2009). The Gaussian distribution function is commonly used (Hofton et al., 2000; Wagner et al., 2006; Reitberger et al., 2008), but other distributions, such as the Generalized Gaussian distribution, the Lognormal distribution (Chauve et al., 2007), the Nakagami distribution or the Burr distribution (Mallet et al., 2010), have been proposed for this task. Other approaches aim at retrieving the differential target cross-section by a deconvolution of the return waveform using the emitted (and recorded) laser pulse. This can be achieved through a Wiener-Filter deconvolution (Jutzi & Stilla, 2006b) or a B-spline deconvolution (Roncat et al., 2011).

By modelling the echoes through waveform decomposition, additional echo attributes can be retrieved. Besides the echo amplitude (in our study referring to the peak amplitude (Wagner et al., 2008b; Mallet & Bretar, 2009; Jörg et al., 2015)), this namely are the energy (i.e. the integral under the return waveform curve (Reitberger et al., 2008; Heinzel & Koch, 2011)), the echo width (Wagner et al., 2006; Reitberger et al., 2008) or the backscatter cross-section (Wagner et al., 2006). However, a calibration step is necessary for the retrieval of the latter attribute.

These echo attributes provide more detailed information about the scatterers and have been shown to be beneficial for classifications of objects. Hence, in addition to structural parameters, which are derived from the 3D echo distribution within the tree crowns, the 1D echo amplitude information (Ørka et al., 2009; Korpela et al., 2010) and the echo energy (Reitberger et al., 2008; Heinzel & Koch, 2011) are typically used for tree species classification. Other studies additionally use the echo width (Reitberger et al., 2008; Lindberg et al., 2014) and the backscatter cross-section (Hollaus et al., 2009) which can be retrieved following the waveform processing approach introduced by Wagner et al. (2006).

Recently, additional waveform analysis approaches for tree species classifications have been introduced where waveform attributes are computed directly from the waveform, without performing a preliminary rigorous decomposition (Yu et al., 2014; Hovi et al., 2016). These approaches showed good results in classifications as well.

The underlying assumption for tree species classification is that the species show distinct signatures in the mentioned echo attributes. Although a wide set of tree properties with influences on the echo attributes has been revealed (Hollaus et al., 2009; Ørka et al., 2009; Korpela et al., 2010; Heinzel & Koch, 2011; Hovi & Korpela, 2014; Hovi et al., 2016), the understanding of how these differences are caused and how the waveform features are modified by the trees is not yet sufficiently advanced (Hovi et al., 2016).

In our study we want to further investigate the potential of full-waveform (FW) ALS data for tree species classification. Namely, we aim at implementing a waveform decomposition which allows for the retrieval of additional 1D echo attributes. Our research objectives are:

1. implement and test a processing chain for the return waveforms such that echo attributes beyond the classically used can be retrieved, e.g. the echo skewness
2. test for differences between the species in the retrieved echo attributes and examine which attributes are the most powerful differentiators
3. quantify the additional value of these echo attributes for species classification

The Gaussian decomposition is used as baseline to compare our results against. Particular attention is paid to the differences of the derived echo attributes between species; the task of this study is not the provision of an elaborate classification framework. Hence, research objective 3 is aimed at the assessment of the potential of echo attributes for tree species discrimination rather than on an improvement of classification accuracy compared to previous studies.

2.2 Materials

2.2.1 Study area

The methods were tested on a 300 x 300 m plot centered at 669 750 E, 259 050 N (CH1903 LV03) on the southern slope of the Laegern ridge in the northeast of Canton Aargau, Switzerland. The terrain is characterized by steep slopes with elevations ranging from 610 to 820 m above sea level. The study area is covered by an old-growth temperate mixed forest, dominated by European beech (*Fagus sylvatica*) and Norway spruce (*Picea abies*). For further details on the test site, see Eugster et al. (2007) and Schneider et al. (2014).

2.2.2 LiDAR data

We used a set of small-footprint full-waveform ALS data acquired under leaf-on conditions on August 1, 2010. For the acquisition, a RIEGL LMS-Q680i (RIEGL Laser Measurement Systems GmbH, Horn, Austria) was used which operates with a wavelength of 1550 nm (Roncat, 2014). The designated mean altitude above ground was 500 m, resulting in a mean footprint diameter of 25 cm on the ground (RIEGL, 2012). The scan angle was limited to ± 15° recorded at a pulse repetition frequency (PRF) of 200 kHz. The return waveform is sampled in an interval of 1 ns.

The pulse width of the emitted laser shot (FWHM$_{sys}$) for Riegl's LMS-Q series is stated to be 4 ns (Reitberger et al., 2008; Roncat, 2014). However, the analysis of the recorded system waveform showed an average FWHM$_{sys}$ of 4.5 ns. This slightly larger width is due to the convolution of the laser pulse with the receiver response function (Wagner, 2010). We used the later measure for the waveform processing, where relevant.

The waveform stored in Riegls's SDF-file format was accessed using the RiWaveLIB (RIEGL, 2013).

For the geocoding process, the smoothed best estimate trajectory (SBET) was available providing the position and the attitude of the sensor at a rate of 200 Hz.

2.2.3 Tree species map

For the investigation of differences between the species in the echo attributes, a tree species map was used. The map was produced based on an ortho-mosaic of 174 geometrically rectified images which was co-registered to a canopy height model (CHM) derived from an ALS dataset. The photographs were taken on October 21, 2013, using an UAV which was operated at a flight altitude of 270 m above ground. This resulted in a spatial resolution of 0.08 m x 0.08 m. For the detection of possible individual tree crowns (ITC), a semi-automatic segmentation approach was employed on the fused set combining the UAV-derived ortho-mosaic and the CHM. The extracted crowns subsequently were visually checked to avoid mixed crowns and crown polygons containing more than a single tree crown were removed. Subsequently, in-situ observations of the tree crowns were matched to the UAV-derived ITCs.

In our study, only the seven most important species were considered. The occurence and number of the trees per species used in the study are declared in Tab. 2.1.

2.2.4 Digital terrain model

A digital terrain model (DTM) of the test site was available. The DTM was created by the data provider (TopoSys GmbH) based on an ALS data set acquired on April 10, 2010. However, the original resolution of 1 m was resampled to a finer resolution of 0.5 m.

2.3 Methods

2.3.1 Waveform decomposition

In this study, we aim at decomposing the return waveform in order to extract additional echo attributes.

The return waveform y of a full waveform laser scanner can be understood as sum of echoes originating from the n targets i at different ranges within the laser's footprint along the flight path of the beam (Hofton et al., 2000):

Table 2.1.: Reference set of mapped trees within the test site with the respective species identifier.

Species name	**trees**	**species group**	**class**
Silver fir (*Abies alba*)	67	conifer	11
Norway spruce (*Picea abies*)	32	conifer	14
Norway maple (*Acer platanoides*)	35	deciduous	22
Sycamore maple (*Acer pseudoplatanus*)	145	deciduous	23
European beech (*Fagus sylvatica*)	396	deciduous	29
European ash (*Fraxinus excelsior*)	208	deciduous	31
Large-leaved lime (*Tilia platyphyllos*)	86	deciduous	56
Total	969		

$$y = f(x) = \sum_{i=1}^{n} f_i(x) \tag{2.1}$$

The aim of this processing step is the decomposition of the return waveform y into single echoes, where each echo is described using a mathematical distribution model $f_i(x)$. Hence, the decomposition step consists first of the determination of the number of echoes within the waveform, including the estimation of initial parameters for the single echo models. Subsequently, the approximated function $f(x)$ as shown in Eq. 2.1 is optimized in order to minimize the difference between the modeled values $f(x_k)$ and the measured waveform sample values y_k of a waveform comprising of N samples (Hofton et al., 2000; Wagner et al., 2006; Reitberger et al., 2008):

$$\sqrt{\frac{1}{N}\sum_{k=1}^{N}\left(f(x_k) - y_k\right)^2} < \epsilon \tag{2.2}$$

This optimization step can be accomplished using, among others, the Levenberg- Marquardt non-linear least-squares method (Hofton et al., 2000; Wagner et al., 2006; Chauve et al., 2007; Reitberger et al., 2008) or constrained non-linear optimization methods as the trust-region algorithm (Lin et al., 2010).

2.3.1.1 Modeling function

Different distribution functions for $f_i(x)$ have been proposed to approximate single echoes composing LiDAR (light detection and ranging) return waveforms. Hofton et al. (2000) used the Gaussian distribution to decompose the waveform of the Laser Vegetation Imaging Sensor (LVIS), which is a large-footprint system. Wagner et al. (2006) demonstrated the use of Gaussians for the decomposition of small-footprint laser scanners to be valid, too. However, this approach assumes that the targets within the laser beam are Gaussian scatterers. Chauve et al. (2007) stated that we can not assume the height distribution of the targets to be Gaussian, which they assumed to be valid for vegetation, too, and proposed the use of the Lognormal and the Generalized Gaussian functions. Mallet et al. (2010) introduced the Nakagami distribution and the Burr distribution as further potential distributions, which in particular allow the modelling of asymmetric echoes. They found that for buildings with more complex geometries comprising skewed surfaces, fitting of skewed distributions is of some eligibility. We assume this to be true for vegetation as well which shows skewed geometries on the scale of the footprint. However, Mallet et al. (2010) further found that also for the more complex geometries, fitting of symmetric distributions was the most accurate solution for a large part of the echoes.

Despite their ability to model asymmetry, these latter functions are not related to Gaussian distributions. However, in this study, we assumed the echoes to be of a general Gaussian shape, but would like to allow for potential asymmetries, probably caused by the tree crown properties and multiple scattering effects.

A feasible function which allows retaining the assumption of Gaussian scatterers but enables the modeling of symmetric as well as asymmetric echoes is provided by the skew normal distribution function (SND) introduced by Azzalini (1985). The function is a composite of the standard normal density function $\phi(x)$ and the standard normal distribution function $\Phi(\alpha x)$, where α controls the shape and, thus, the skewness of the density distribution. The function is composed as:

$$f(x|\alpha,\omega) = 2\phi(x)\Phi(\alpha x) \tag{2.3}$$

where:

$$\phi(x) = \frac{1}{\sqrt{2\pi}} e^{-\frac{x^2}{2}} \tag{2.4}$$

and

$$\Phi(x) = \int_{-\infty}^{x} \phi(t)\,\mathrm{d}t = \frac{1}{2}\left[1 + erf\left(\frac{x}{\sqrt{2}}\right)\right] \tag{2.5}$$

with *erf* denoting the error function. In order to control the scale and the position of the function on the waveform, parameters for the amplitude *A*, the scale ω and the location *s* on the time axis were added. With this added modifications, the function was implemented as:

$$f(x|A,s,\alpha,\omega) = A\frac{2}{\omega}\frac{1}{\sqrt{2\pi}} exp\left(-\frac{\left(\frac{x-s}{\omega}\right)^2}{2}\right)\frac{1}{2}\left[1 + erf\left(\alpha\frac{\left(\frac{x-s}{\omega}\right)}{\sqrt{2}}\right)\right] \tag{2.6}$$

where the resulting distribution is left-skewed for negative α, symmetric for $\alpha = 0$ and right-skewed for positive α.

Additionally to the SND decomposition, a Gaussian decomposition was performed using the Normal distribution function with amplitude *A*, position *s* and width parameter σ (MathWorks, 2016b):

$$f(x|A,s,\sigma) = A\left(\frac{1}{\sqrt{2\pi\sigma}}\right) exp\frac{-\left(x-s\right)^2}{2\sigma^2} \tag{2.7}$$

2.3.2 Waveform processing

The entire waveform processing was performed on the raw, uncorrected return waveform. Riegl's LMS-Q series records the return waveform in two channels with different sensitivities (RIEGL, 2014). In this study, only the linear operating low power channel was used. The high power channel was skipped for lack of further information regarding the mode of operation. For our data set, this corresponds to a reduction of processed waveforms of 12.8% with respect to the total number of waveforms recorded.

To facilitate the subsequent comparison of echo amplitude and energy values, the waveform was normalized to a defined mean range as described in Höfle & Pfeifer (2007). With this procedure, the largest part of the intensity differences inbetween waveforms are already eliminated (Jörg et al., 2015).

2.3.2.1 Echo detection and initial parameters

For echo detection, only waveform samples exceeding a noise level of 6 DNs in the unnormalized waveform were considered. This noise level is used in other studies with Riegl's LMS-Q series as well (Reitberger et al., 2008; Mallet, 2010).

Waveform analysis for echo detection was performed in two steps. First, the local maxima were detected based on the zero crossings of the first derivative (Wagner et al., 2004; Chauve et al., 2007). However, as pointed out by Chauve et al. (2007), this echo detection method is insufficient in case of complex waveforms with overlapping echoes. To overcome this deficiency, overlapping peaks were detected in a second step based on the approach described by Lin et al. (2010). Around each detected echo from step one, groups of waveform samples exceeding the noise level were created. For each of these groups, the second derivative was calculated in order to find inflection points. Additionally detected echoes at the inflection points were kept if their amplitudes exceeded 1/5 of the related first-derivative echo and if the temporal spacing between these two echoes exceeded the sensor's range resolution, i.e. half the width of the system waveform (Baltsavias, 1999).

For both, the Gaussian and the SND decomposition, the locations of the detected echoes on the waveform were used as initial estimates for the echo locations. The initial amplitude was set to the amplitude of the echo. For the Gaussian decomposition, the initial echo width was set to the width of the system waveform (Mallet, 2010), while the initial echoes for the SND decomposition were set to symmetric shapes ($\alpha = 0$) and left unscaled ($\omega = 1$).

2.3.2.2 Waveform decomposition

The Levenberg-Marquardt method used for the curve fitting in previous studies is an unconstrained least-squares approach (Hofton et al., 2000; Wagner et al., 2006; Reitberger et al., 2008). Hence, it may lead to invalid echo parameters such as negative echo amplitudes and was found to fail to find a solution at all in some cases (Wagner et al., 2006). However, in the case of modeling the return waveform from small-footprint laser scanners, certain value ranges for the echo parameters can be assumed. Hence, as suggested in Lin et al. (2010), the trust-region algorithm by Coleman & Li (1996), already implemented in MATLAB (2014), was chosen for the curve fitting. The algorithm is a constrained non-linear optimization approach allowing for the definition of lower and upper bounds for each of the echo parameters to be found in the curve fitting process (MathWorks, 2016a).

2.3.2.3 Echo removal

Although the deployed trust-region optimization approach leads to limited parameter ranges, the echo parameters were checked regarding the assumed parameter ranges before an echo was retained. Only echoes with a full width at half maximum (FWHM) larger than 0.7 times (Lin et al., 2010) and a maximum of two times $FWHM_{sys}$ were kept. Furthermore, the amplitude was ensured to exceed the noise level and the spacing between two consecutive echoes was verified to be larger than the range resolution. Echoes violating one of these criterions were discarded.

A second type of echoes unaffected by the constraints introduced in the trust-region optimizer regards echoes induced by the so-called ringing effect as described in Roncat et al. (2008). These echoes do not necessarily show invalid parameters but are induced by the sensor electronics in the presence of strong echoes in the return waveform. Echoes from ringing are estimated to occur 10 to 14 ns after a strong echo. Furthermore, this echo type is expected not to exceed an amplitude ratio of 1/5 (Roncat et al., 2008) to 1/13 (Lin et al., 2010) of the amplitude of the penultimate echo. In this study, a ratio of 1/10 was chosen, which is a slightly more conservative approach compared to Roncat et al. (2008).

2.3.2.4 Echo attributes

For the Gaussian and the SND model, the amplitude A, the energy E and the FWHM were computed. Additionally, in the case of the SND decomposition, the third and fourth statistical moments of the distribution of each echo, i.e. the skewness and the kurtosis, were calculated as in Azzalini (1985):

$$skew = \frac{4-\pi}{2} \frac{\left(\delta\sqrt{2/\pi}\right)^3}{\left(1-\frac{2\delta^2}{\pi}\right)^{3/2}} \tag{2.8}$$

$$kurt = 2\left(\pi-3\right) \frac{\left(\delta\sqrt{2/\pi}\right)^4}{\left(1-\frac{2\delta^2}{\pi}\right)^{2}} \tag{2.9}$$

where

$$\delta = \frac{\alpha}{\sqrt{1+\alpha^2}} \tag{2.10}$$

Using the depicted formula for the calculation of the kurtosis, the values are relative to the Gaussian distribution, i.e. the Gaussian distribution in this case has a kurtosis of 0.

Furthermore, as no radiometric calibration was performed on the laser measurements, the amplitude and energy values have to be considered as relative values, which only allow for the cross-comparison of measurements from the same flight campaign.

2.3.3 Attribute aggregation

For each tree, the echo attributes were spatially aggregated in order to enable a meaningful comparison across the species regarding variations in the echo characteristics. From the attribute aggregation per tree crown, we anticipate to achieve a more distinct species-dependent signature, and to compensate for a certain amount of influence of the scan angle on the echo shape on the other hand.

For aggregation, the mean and the standard deviation of each attribute per ITC were calculated (Torabzadeh et al., 2014). This was done on two vertical scales, namely on full crown level and on decile level, respectively. For the decile level aggregation, each ITC was divided evenly into ten layers (*d1...d10*).

The ITCs were extracted from the point cloud using the tree species map described in section 2.2.3. As in Torabzadeh et al. (2014), all echoes above a height of 3 m above ground were considered to be canopy echoes.

The aggregation was done separately for all echoes originating from the canopy (*all*-echoes) and for solely the first (*first*)-echoes. As first echoes are not affected by transmission losses from backscattering on previous targets, they are generally stronger and less noisy (Korpela et al., 2012). The separate analysis of the echo types is adapted from Hovi et al. (2016).

An overview of the denotation of the derived products as used in later evaluation steps is depicted in Tab. 2.2.

2.3.4 Structural features

Additionally to the echo attributes, the relative-frequency distribution (RFD) (Leiterer et al., 2015) of the echoes within the canopy was calculated to obtain a feature space of higher dimension for the classification. However, according to Korpela et al. (2010), the canopy was divided into deciles rather than using an absolute bin hight. For every decile, the respective number of echoes in relation to the total number of canopy echoes was calculated seperately for *all*-echoes (*all_RFD*) and *first*-echoes (*first_RFD*), respectively.

2.3.5 Statistical methods

To assess the value of the additional attributes, the aggregated echo attributes were tested for significant differences between the species using an analysis of variance (ANOVA). This was done for each species pair deploying the function *anova* which is already implemented in the R package *stats* (R Development Core Team, 2016). For all evaluations, a $p = 0.05$-level of significance was used.

Furthermore, we run a random forest (RF) classifier (Breiman, 2001) which is a non-parametric classifier. RFs bring the advantage of providing an estimate of the attribute importances based on the trained decision trees. This is, besides the actual classification, RFs additionally evaluate the discrimination power of the echo attributes which in this

Table 2.2.: Product name compounds for the aggregations of different return types, attributes, statistical measures and aggregation levels. For example, *all_A_std_canopy* is the standard deviation of the amplitude values of all echoes (i.e. all returns within the tree crown) aggregated on canopy layer.

return type	echo attribute	aggregation type	aggregation level
all, first	*A, E, fwhm, skew, kurt*	*mean, std*	*canopy, d#*

study was a key interest. However, for the RF runs, only the attribute importances were of interest while the classification power was not regarded.

We used the MATLAB implementation of RF (*TreeBagger*). The tree depth was set to e a minimum of one observation per tree leaf while the number of decision trees which are trained was set to 128, as for a larger number of trees, the classification accuracy was reported to only show little increase (Oshiro et al., 2012).

2.3.6 Species classification

In order to test the benefit of the additionally computed echo attributes energy, FWHM, skewness and kurtosis over the use of solely the echo amplitude, three classification runs using three sets with different attribute spaces were performed. In the first run, only the echo amplitude attributes were used. For the second run, the energy and FWHM attributes were added and in a third run, all derived echo attributes have been used. For each attribute, the crown aggregates from *first*- and *all*-echoes were considered. The structural information calculated from *all*-echoes (all_RFD) and *first*-echoes ($first\_RFD$), respectively, were used as auxiliary features in order to enlarge the feature space. The classification power was assessed based on the overall accuracy (OA), Cohen's κ, producer's (PA) and user's accuracy (UA).

The separation of the classified trees into a test set and a training set, respectively, was done individually for each species where half of the total number of trees per species was selected randomly as training set while the other half was retained as test set. Separate division for each species guarantees an even partition of the trees of each species which is important as the number of trees per species differs widely (Tab. 2.1).

We deployed a support vector machine (SVM) classifier. This classifier has been found to outperform other classification methods regarding the achieved accuracies in applications with high dimensional data-sets and small numbers of training samples (Melgani & Bruzzone, 2004; Pal & Mather, 2006) and has been applied on LiDAR data sets before (e.g. Koetz et al., 2008; Mallet et al., 2010; Torabzadeh et al., 2014).

For the classification, the LIBSVM package by Chang & Lin (2011) was used, which provides a MATLAB interface.

2.4 Results

2.4.1 Decomposition performance

As the same echo detection approach was chosen for the SND and the Gaussian decomposition, the resulting point clouds of both decompositions are similar regarding the number of detected echoes per waveform and, hence, regarding the point density within the test site (Tab. 2.3). However, differences in the decomposition and the echo attributes emerge.

Table 2.3.: Echo assessment for SND and Gaussian decomposition for the entire test site. The assessment bases on the uncorrected point cloud which comprises echoes below ground.

	SND	Gaussian
computed pulses	2’494’019	2’583’879
number of echoes	9’176’365	9’236’544
average point density [pts/m^2]	101.28	101.95
median number of echoes per pulse	4	4
ratio of *first*-echoes	30.59%	31.41%
ratio of only echoes	5.02%	6.00%
average RMSE	5.084	4.050

2.4.1.1 Differences in decomposition

Fig. 2.1 demonstrates the decomposition of a return waveform originating from a Silver fir (*Abies alba*) using SND and Gaussian distribution functions, respectively. In the example, the SND decomposition fits the return waveform in a more sufficient way while the Gaussian decomposition shows deficiencies in modeling all echoes appropriately. In addition, the figure illustrates differences in the echo shapes as the SND is able to model skewed energy distributions of the echoes (Fig. 2.1c, depicted in red). However, most of the return echoes of the SND decomposition are of almost symmetric shape (i.e. skewness = 0) (Fig. 2.2). Hence, the skewness feature for the single trees is of small magnitude when aggregated on canopy level (Fig. 2.6).

Overall, the Gaussian decomposition shows a better performance regarding the RMSE as the error of the SND decomposition is slightly higher on average ($RMSE_{Gaussian} = 4.050$, $RMSE_{SND} = 5.084$, Tab. 2.3).

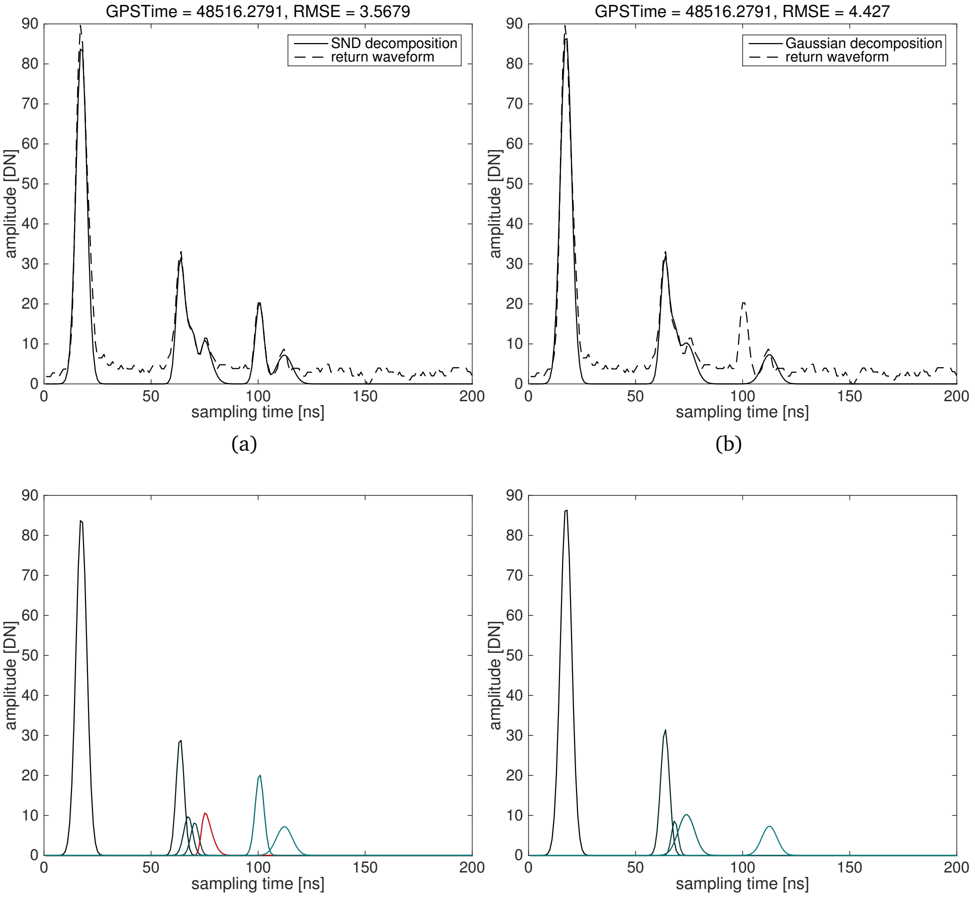

(a) (b)

(c) (d)

Figure 2.1.: Waveform from a Silver fir tree fitted with SND (left) and Gaussian (right) distribution functions, respectively. Top row: measured return waveform (dashed line) with fitted waveform (solid line) from the two decompositions. Bottom row: single echoes as fitted by the decompositions with visible skewed echo (red) in Fig. 2.1c from the SND decomposition. In this example, the SND decomposition shows a better performance resulting in a smaller RMSE.

2.4.1.2 Differences in echo attributes

Differences between the decompositions occur in the echo attributes when aggregated at crown-level. The Gaussian decomposition fits echoes with larger amplitudes, energies and FWHMs in general compared to the SND decomposition (Fig. 2.3, top row). The differences between the two model functions are significant at a $p = 0.05$-level for all three echo attributes. However, the attributes are highly correlated (Fig. 2.3, bottom row).

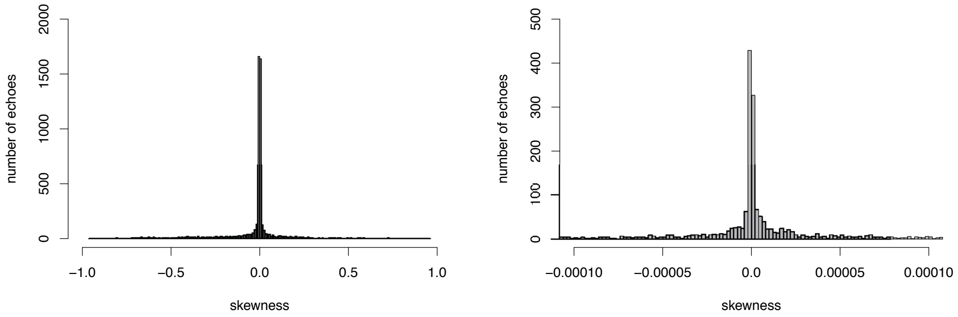

Figure 2.2.: Distribution of the skewness values of the $N = 5530$ echoes originating from a single Silver fir (*Abies alba*) tree considering *all*-echoes of the crown. Depicted is the entire skewness range (left) and the the skewness range around 0 only (right). For better illustration, the number of bins is increased in the right plot.

2.4.1.3 *Distribution of echo types*

Fig. 2.4 shows a single Silver fir (*Abies alba*) subsetted from the entire point cloud. As visible, the decomposition detects echoes below ground (depicted in red), as the terrain information was not used in the decomposition. However, as only canopy returns ($>$ 3 m above ground) are considered in the aggregation, these echoes are excluded.

The separation of the point cloud into *first*-echoes and *all*-echoes results in sufficiently large point clouds for both echo types for each tree on average (Tab. 2.4). The height distribution of the reflecting points of the two echo types (Fig. 2.5) illustrates the *first*-echoes to originate from the top of the crown rather while the lower parts are covered by *all*-echoes. However, it has to be emphasized that the *first*-echoes are a sub-category of *all*-echoes and, thus, are also contained in the latter group.

2.4.2 *Species differentiation*

2.4.2.1 *Differentiation power*

The set of seven species, which we aim to discriminate, results in 21 possible combinations of species pairs which have to be compared to one another. Considering all echo attributes derived from the SND decomposition, the evaluation reveals good discriminability of coniferous and deciduous trees in general, as every deciduous species differs from coniferous species in multiple attributes. Regarding the differences in the aggregated attributes of the single species, Norway maple, Sycamore maple and Large-

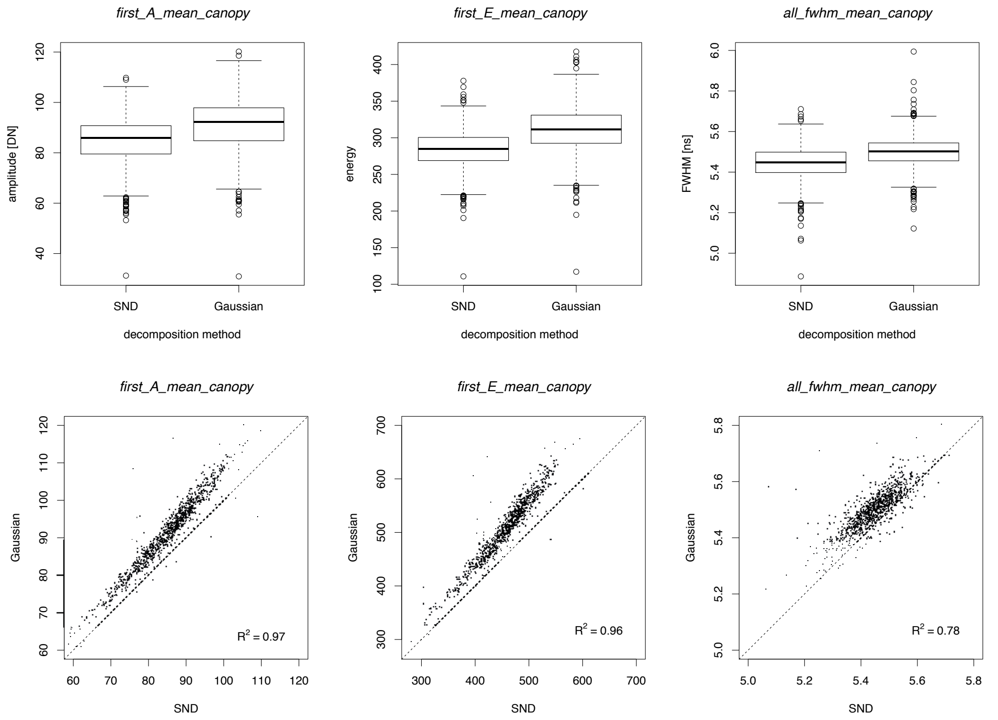

Figure 2.3.: Top row: Comparison of the value ranges of the crown aggregated echo attributes amplitude, energy and FWHM, respectively, for the two decompositions. Bottom row: Correlation of the aggregated echo attributes between the SND and the Gaussian decomposition for the set of 969 trees.

Table 2.4.: Number of average echoes per echo type and tree, reported separately for each species and decomposition approach.

species	*all*-echoes		*first*-echoes	
	SND	Gaussian	SND	Gaussian
11	3949.2	4017.3	1370.1	1407.8
14	3426.1	3500.1	1138.2	1169.4
22	1535.9	1555.4	467.5	480.9
23	2580.2	2634.5	787.8	813.7
29	3069.6	3113.8	925.4	955.9
31	2930.1	2978.0	928.0	954.2
56	1831.9	1869.8	557.0	573.8

leaved lime show the least distinct signatures, resulting in lower numbers of attributes in which they differ from other species (Tab. 2.5). Norway maple shows a huge overlap to European beech (no differences in any attribute), as well as to Large-leaved lime (one significantly differing attribute) and Sycamore maple (three significantly differing

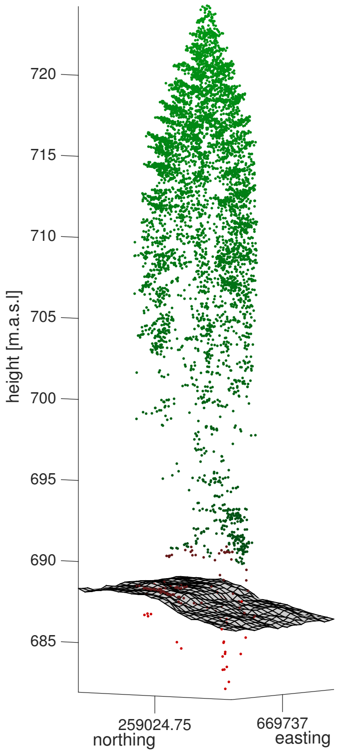

Figure 2.4.: Subset of a single Silver fir tree from the point cloud from the SND decomposition. The point cloud is segmented into the canopy layer (green), the underwood layer (brown) and into a layer consisting of false echoes detected below ground (red). For clarification, the terrain is depicted in gray.

attributes). A further huge overlaps was found between Large-leaved lime and Sycamore maple (two significantly differing attributes).

Fig. 2.6 depicts the value ranges of the crown aggregated echo attributes for each species for the data set from the SND decomposition. For each attribute the echo type showing the highest count of significant differences in the mean is shown. Tab. 2.6 reports the number of significantly differing species for the crown-aggregates. This reveals the discrimination power of the respective attributes.

The most differences are present in the mean energy and the mean amplitude of the *first*-echoes and the skewness of *all*-echoes (in order of decreasing number of differing species). An intermediate position has the standard deviation of the energy of *all*-echoes and the FWHM of *first*-echoes, respectively.

Regarding the statistical type of the aggregation, the mean aggregates reveal more between-species differences than the aggregates based on the standard deviation.

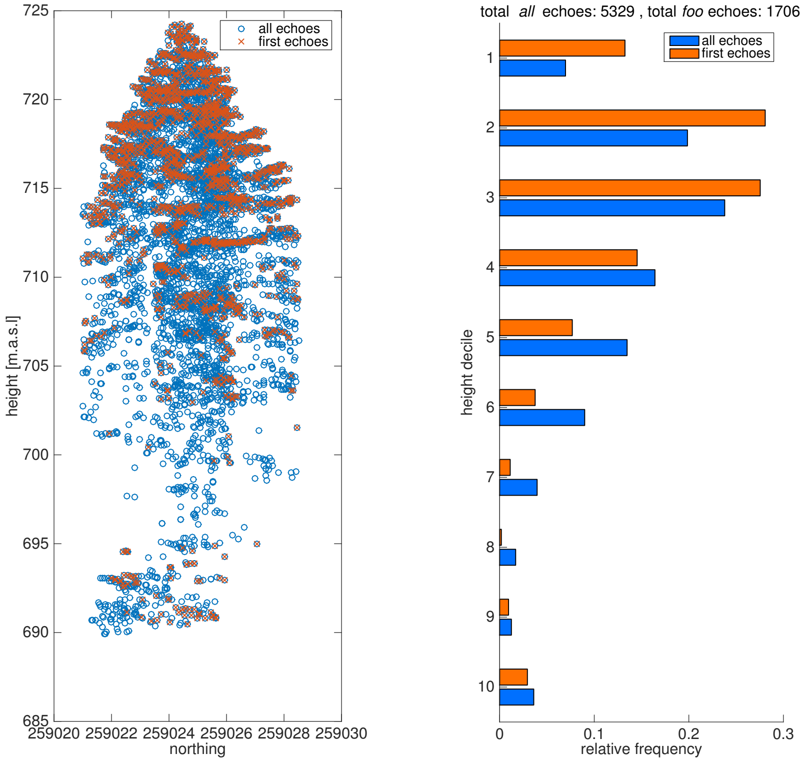

(a) (b)

Figure 2.5.: Canopy subset taken from the point cloud depicted in Fig. 2.4. Left: 2D plot of the canopy illustrating the origin of *all*- (blue) and *first*-echoes (orange), respectively, from within the canopy layer. Right: relative frequency distribution (RFD) of the two echo types within the deciles of the canopy.

Furthermore, it becomes apparent that the number of between-species variations differ across the echo types. *all*-echoes comprise more information in the skewness while *first*-echoes contain a higher differentiation power in the amplitude, energy and FWHM, when considering the mean aggregates. For the standard deviation, the aggregated attributes show better performance for the *first*-echoes in general.

Considering the species types, coniferous species tend to be characterized by echoes of lower amplitude and energy, narrower widths and of more symmetric shapes in general. However, the attribute ranges of the trees overlap hugely and this finding is more distinct for Norway spruce than for Silver fir, which is closer to the deciduous species.

2.4.2.2 Attribute importance

A complementary measure to the count of significant differences is the attribute importance as provided by the RF. This measure reports how descriptive an attribute is for

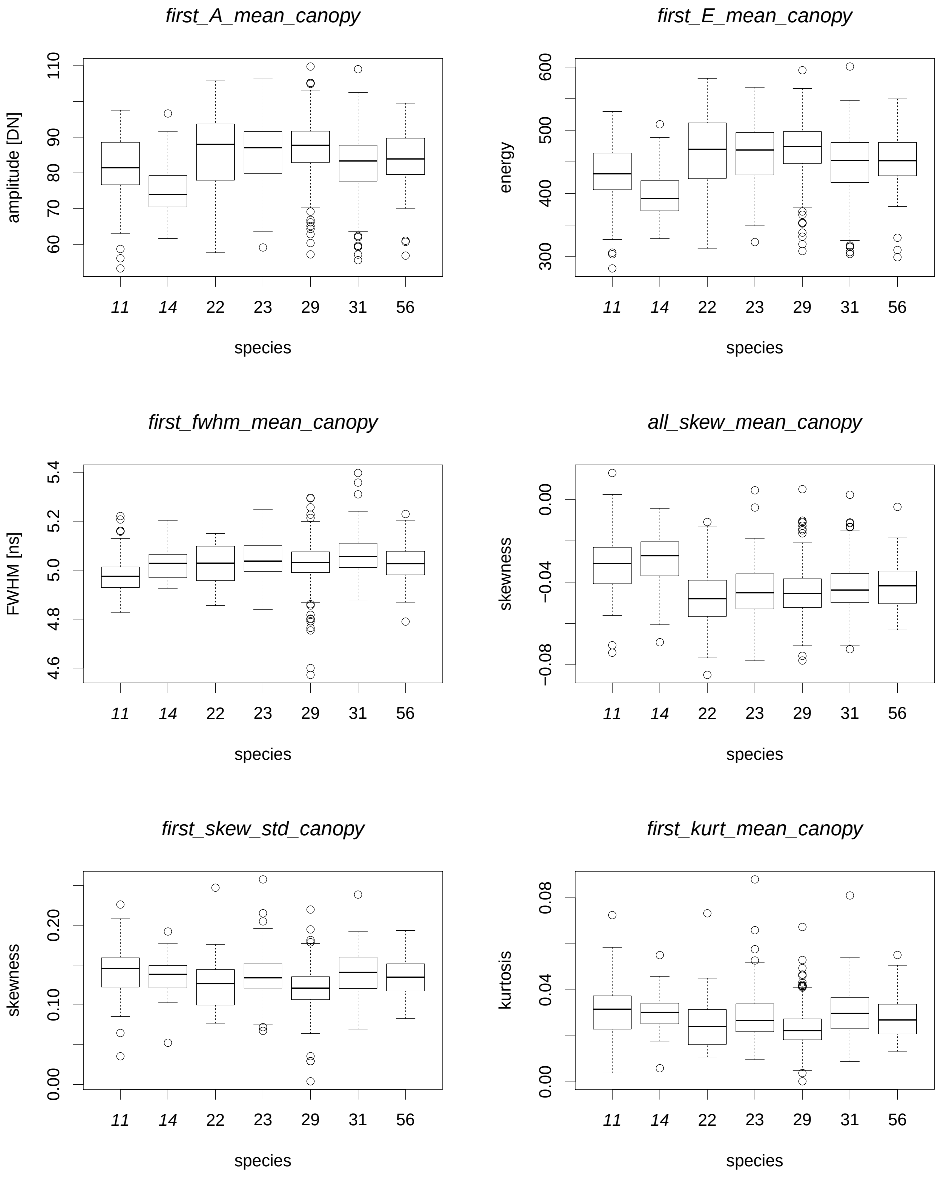

Figure 2.6.: Differences between the species in the echo attributes of the SND decomposition, aggregated on canopy level. For each attribute, the mean aggregates for the echo type containing the highest count of differing species is depicted. Additionally, the standard deviation of the aggregated skewness ranges of the first echoes is shown. Species identifiers of conifers are written in italic letters. The significance of the differences is reported in Tab. 2.6.

species discrimination in the classifier. The importance was assessed based on 50 classification iterations for each attribute set from the SND decomposed data. The top ten

Table 2.5.: Summary of the discriminability in the canopy aggregates of the seven species for the SND decomposed data set. For each species, $\sum$ *differences* sums up the number of significant differences to other species for all attributes (theoretical maximum = (7-1) species · 10 attributes = 60). *total differences* sums up the sum of differences from both aggregation types for each species. A higher value indicates the species to show a more distinct signature in the attributes. Additionally, the number of species with differences to the respective species in any of the attributes is reported as *sep. species*. A value of 6 means, that the respective species differs from any other species in at least one attribute.

	mean		*std. dev.*		
species	$\sum$ differences	sep. species	$\sum$ differences	sep. species	total differences
11	35	6	19	6	54
14	39	6	20	6	59
22	19	4	17	4	36
23	21	5	22	5	43
29	33	5	32	5	64
31	32	6	30	6	62
56	24	6	23	5	47

attributes occurring the most frequent among the ten best performing attributes in the 50 iterations are reported in Tab. 2.7. However, the analysis is a qualitative measure only, not accounting for the between-species variation explained by the respective attributes. Nonetheless it reveals a certain value of the attributes for the classification.

For the first attribute set comprising of the echo amplitude only, structural features measured as relative frequency distribution (*RFD*) are of relatively high importance. When the echo energy and the FWHM are added, a shift towards these attributes can be observed, while amplitude attributes still are selected. In the third run using the attribute set additionally comprising of echo shape related parameters, i.e. the skewness and the kurtosis, these parameters have higher discrimination power in the classifier and are selected the most often.

2.4.3 *Attribute dependencies*

2.4.3.1 *Influence of height*

A first group of possible impacts on the echo attributes relates to tree specific properties, i.e. properties that are not dependent on the species but unique for each individual tree. By analysing the correlation between the echo attributes and tree-specific influences, we retrieve a measure, which could explain a certain amount of the intra-species variation

Table 2.6.: Summary of the ANOVA test for significant differences between species pairs for each echo attribute and echo type, distinguished in regard to the aggregation metrics on canopy level. The evaluation is done on a $p = 0.05$ significance level, the number of trees is $N = 969$. For seven species, the maximum number of 21 combinations (pairs) are possible, which could theoretically be separated per attribute.

attribute	number of differences between species	
	mean	*std. dev.*
all_A_canopy	8	8
all_E_canopy	9	12
all_fwhm_canopy	10	0
all_skew_canopy	14	6
all_kurt_canopy	7	8
first_A_canopy	14	9
first_E_canopy	15	7
first_fwhm_canopy	11	12
first_skew_canopy	7	8
first_kurt_canopy	7	8

of the respective attributes. However, in our case, little knowledge on individual tree properties was available. Hence, only the correlation to the tree height could be analysed.

We found large differences of the height influence for a given attribute between the species (Tab. 2.8). For the three species, for which we subsequently performed a classification, the correlation of the FWHM (*all_fwhm_mean_canopy*) and the skewness (*all_skew_mean_canopy*), respectively, and the tree height are depicted (Fig. 2.7). The figures clarify the huge overlap of the three species and the wide intra-species variation which was already seen in Fig. 2.6.

2.4.3.2 *System waveform and scanning angle impact on echo skewness*

A second group of impacts corresponds to impact factors introduced by the sensor, survey configuration or in the curve fitting step, respectively. In order to get an estimate of the bias in the detected echo skewness, we assessed if and how this attribute is affected by non-tree specific impacts.

Fig. 2.8 depicts the relation of echo skewness to the energy and the FWHM, respectively. The assessment reveals no strong correlations for the echo attributes in both return types ($R^2 = 0.15$ for *all_energy*, $R^2 = -0.08$ for *all_fwhm*, $R^2 = 0.11$ for *first_energy*, $R^2 = 0.15$

Table 2.7.: Attributes showing the highest frequencies amongst the ten best performing attributes selected by the RF in 50 classification iterations using different attribute sets from the SND decomposition. Occurrences report, how many times the respective attribute is chosen among the ten best attributes.

	A		*A, E, FWHM*		*A, E, FWHM skew, kurt*	
rank	attribute	occurrence	attribute	occurrence	attribute	occurrence
1	*first_A_mean_canopy*	42	*first_fwhm_std_canopy*	45	*first_kurt_mean_canopy*	48
2	*all_RFD_d1*	39	*first_A_mean_canopy*	37	*first_skew_std_canopy*	46
3	*all_RFD_d10*	37	*first_E_mean_canopy*	28	*first_kurt_std_canopy*	44
4	*all_A_mean_canopy*	31	*all_E_std_canopy*	27	*all_kurt_std_canopy*	33
5	*all_RFD_d3*	31	*all_RFD_d3*	27	*first_E_mean_canopy*	30
6	*all_A_std_canopy*	29	*all_RFD_d9*	27	*first_A_mean_canopy*	29
7	*first_RFD_d3*	29	*first_RFD_d6*	26	*first_fwhm_std_canopy*	29
8	*first_RFD_d1*	27	*all_A_std_canopy*	25	*all_skew_std_canopy*	23
9	*first_RFD_d7*	27	*all_RFD_d1*	22	*all_E_mean_canopy*	22
10	*all_RFD_d9*	24	*first_RFD_d2*	21	*all_A_mean_canopy*	19

Table 2.8.: Dependency of the echo attributes on the tree height for the echoes aggregated on canopy layer. Depicted are the mean values of the single trees of the three species comprising of the highest number of individuals within the site which are later used for the classification.

	all_A	*first_A*	*all_E*	*first_E*	*all_fwhm*	*first_fwhm*	*all_skew*	*first_skew*	*all_kurt*	*first_kurt*
Sycamore maple	-0.12	-0.17	-0.12	-0.18	0.06	0.07	0.13	0.04	0.06	0.26
European beech	-0.09	-0.06	-0.09	-0.07	0.08	0.07	0.05	0.11	0.03	0.19
European ash	-0.21	-0.09	-0.22	-0.12	0.14	-0.08	0.06	0.00	0.08	0.23

for *first_fwhm*), but indicates a limitation in the echo skewness range for increasing echo width.

The system waveform shows some temporal variability in respect to skewness, but this has little impact on the skewness of the echoes ($R^2 = -0.011$, Fig. 2.9). Regarding the acquisition geometry, we found that the skewness is only very weakly correlated with the scan angle ($R^2 = 0.047$).

2.4.3.3 Vertical variation of echo attributes within the canopy

Fig. 2.10, Fig. 2.11 and Fig. 2.12 show vertical variation of the amplitude, the FWHM and the skewness, respectively, in terms of per decile aggregated echoes within single tree crowns.

The amplitude of *first*-echoes decreases with increasing penetration depth into the crown, i.e. with decreasing deciles (Fig. 2.10a). Furthermore, an increase in the value range of the decile-wise aggregated amplitude values for the individual species can be

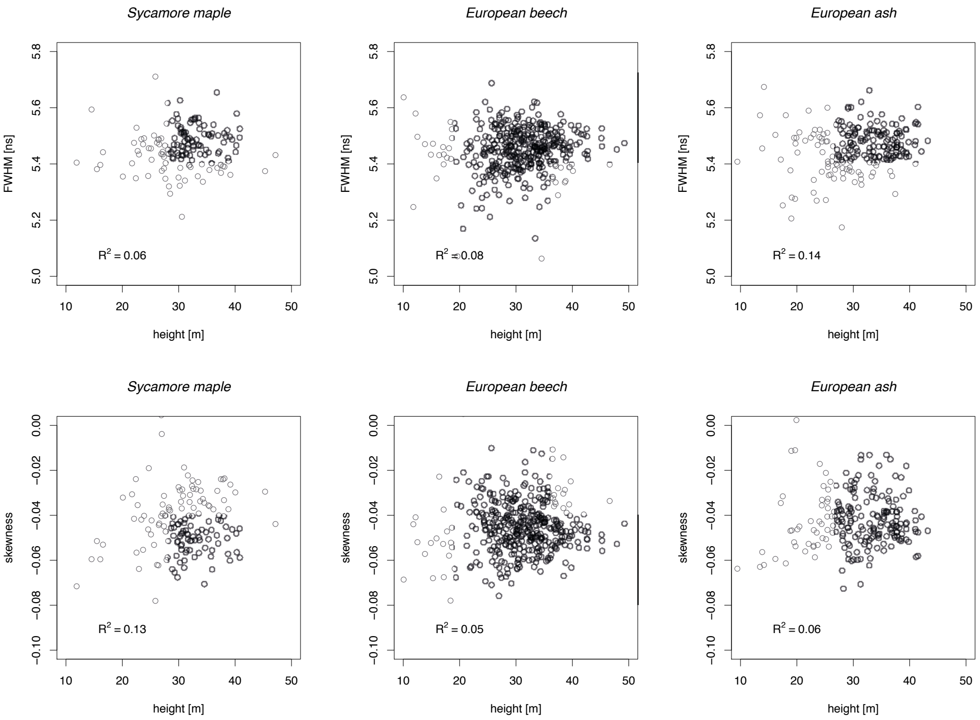

Figure 2.7.: Correlation between the tree height and the FWHM (*all_fwhm_mean_canopy*, top) and the skewness (*all_skew_mean_canopy*, bottom) for Sycamore maple, European beech and European ash, respectively.

observed (Fig. 2.10b, 2.10c). The vertical variation of the energy of the *first*-echoes is similar, although not depicted here.

The mean aggregated skewness decreases from the top to the bottom of the tree crown (Fig. 2.12a), i.e. the aggregated echoes become increasingly more symmetric. This is true for all species within the top 70% of the tree crown. For the lower 30% of the crown, the findings diverge, showing deflections to larger negative values in single deciles for some species. For the lowest decile, the averaged aggregations per species are positive (0.011 - 0.031), however with the exception of Norway spruce (-0.029).

A better impression of the vertical variation of the skewness can be achieved by tracing the ranges of the echo skewness values per decile (i.e. *all_skew_mean_d#*) for the single tree species (Fig. 2.12b, 2.12c). This reveals a widening of the skewness with increasing penetration depth into the crown. This behaviour is also reflected in the range of the standard deviations of the skewness, which increases with decreasing height of the decile (Fig. 2.12d, 2.12e). The observed effect is smaller for the Silver fir than for the European beech and is more distinct for deciduous trees than for coniferous trees in general.

The vertical variation of the aggregated FWHM averaged per species (*all_fwhm_mean_d#*) shows an increase, i.e. a widening, with decreasing decile height for the top 70% of the tree crown in general (Fig. 2.11a). For the lower 30% of the crown, the FWHM slightly decreases again (*all_fwhm_mean_d*$1 = 5.17 - 5.26$ ns, *all_fwhm_mean_d*$7 = 5.56 - 5.73$ ns, *all_fwhm_mean_d*$10 = 5.50 - 5.60$ ns), except for Norway maple and Large-leaved lime (*all_fwhm_mean_d*$1 = 5.22$ ns and 5.23 ns, resp., *all_fwhm_mean_d*$7 = 5.56$ ns and 5.67 ns, resp., *all_fwhm_mean_d*$10 = 5.63$ ns and 5.75 ns, resp.). These two species do not have a distinct vertical variation in their echo properties.

The vertical profile of the FWHM per species in Fig. 2.11a follows the same general form as the aggregated FWHM of the single trees of the same species (Fig. 2.11b, 2.11c). The echo width aggregated on decile level increases with decreasing canopy decile height for the top 70% of the canopy, but subsequently shows the observed decrease for the lower deciles. As for the skewness, the widening of the FWHM range is more distinct for the European beech and for deciduous species in general, than for the Silver fir and the coniferous species.

However, it has to be emphasized that the lower 30% of the crown comprise of only 6.7% of the echoes when averaging over all evaluated tree crowns. Hence, the values for the upper layers might be more robust.

2.4.4 Classification performance

For the classification, the crown aggregated attributes derived from the SND decomposition were considered. Only the classification results from the SVM classification were evaluated.

The classification was deployed for two different tasks. First a differentation of coniferous and deciduous trees was performed. In a second classification, which was independent from the first, we aimed at classifying a species set comprising of the three largest species groups, that is, Sycamore maple, European beech and European ash. For the other four species, we considered the number of individuals within the test site to be too small to provide robust results.

In order to achieve a robust estimation of the classification performance, 50 classification iterations have been performed, using a different training and test set in each iteration.

The mean classification power for the differentiation of coniferous and deciduous trees for the different attribute sets is depicted in Tab. 2.9. The differentiation shows good results in general and benefits from the additional echo attributes. This is true particularly for the accuracy measured as Cohen's κ, which shows a larger improvement than the overall accuracy (0.611 vs. 0.389 for Cohen's κ, 93.45% vs. 89.76% for the overall accuracy). However, the main increase in the accuracy is observed when the energy and the FWHM are added (0.570 vs. 0.389 for Cohen's κ, 92.96% vs. 89.76% for the overall accuracy) while the use of additionally the skewness and the kurtosis does not improve the accuracy to the same magnitude anymore (0.611 vs. 0.570 for Cohen's κ, 93.45% vs. 92.96% for the overall accuracy).

The species classification, too, shows an improvement in terms of the overall accuracy (59.74% vs. 55.95%) and of Cohen's κ (0.256 vs. 0.202) when additional echo attributes are added to the feature space (Tab. 2.11). However, the classification performance is only mediocre in general.

Considering the producer's (PA) and the user's accuracies (UA), the findings for the improvements are inconsistent (Tab. 2.12). While the UA increases with every added attribute, only the PA of the two larger groups (i.e. European beech and European ash) increases, when using the larger attribute set, while the PA for the smallest group (Sycamore maple) decreases.

Table 2.9.: Performance of the differentiation of coniferous and deciduous trees for 50 classification iterations. Depicted is the mean classification performance measured as overall accuracy (*OA*) and Cohen's κ for each attribute set. Overall accuracy values are in [%].

	A	*A, E, FWHM*	*A, E, FWHM skew, kurt*
OA	89.76	92.96	93.45
Cohen's κ	0.389	0.570	0.611

2.5 Discussion

2.5.1 Deriving additional echo attributes (RQ1)

Waveform decomposition using the Gaussian distribution function is a well known problem. The implemented decomposition method shows a comparable performance to other

Table 2.10.: Mean producer's and user's accuracies for the differentiation of coniferous and deciduous trees. All values are in [%].

	A		*A, E, FWHM*		*A, E, FWHM skew, kurt*	
	PA	UA	PA	UA	PA	UA
coniferous	40.65	49.98	54.00	70.61	59.14	71.94
deciduous	95.29	93.45	97.35	94.95	97.31	95.49

Table 2.11.: Performance of the tree species classification for 50 classification iterations. Depicted is the mean classification performance measured as overall accuracy (*OA*) and Cohen's κ for each attribute set. Overall accuracy values are in [%].

	A	*A, E, FWHM*	*A, E, FWHM skew, kurt*
OA	55.95	57.56	59.74
Cohen's κ	0.202	0.231	0.256

studies when regarding the RMSE (e.g. Armston et al., 2013). The accuracy of the SND decomposition is slightly smaller, but still in the same range ($RMSE_{Gaussian} = 4.050$, $RMSE_{SND} = 5.084$). Thus, using the Gaussian decomposition as baseline, we attest the general feasibility of performing a SND decomposition.

Using the SND function for the decomposition allows the retention of the assumption of Gaussian scatterers (Wagner et al., 2006). As we found a large part of the echoes to be of symmetric shape, this assumption can not be discarded. On the other hand, no limitations regarding the echo skewness are introduced by using the SND function.

However, compared to the implemented Gaussian decomposition the echoes derived

Table 2.12.: Mean producer's and user's accuracies of the species classification. All values are in [%].

tree species	*A*		*A, E, FWHM*		*A, E, FWHM skew, kurt*	
	PA	UA	PA	UA	PA	UA
Sycamore maple	14.03	28.88	12.44	31.53	9.03	35.80
European beech	81.32	61.00	82.70	62.29	87.15	62.88
European ash	36.65	51.06	40.94	52.65	42.65	55.05

from the SND decomposition show smaller amplitude, energy and FWHM values, respectively. The cause for this is not entirely clear, as the majority of the fitted echoes from the SND decomposition is of almost symmetric shape, i.e. Gaussians. Yet, the respective attributes from both decompositions are highly correlated. Hence, as only the relative measures from the same flight campaign are considered in the comparison across the species, these relative shifts should result in an absolute bias. If the aim would be to allow for a comparison across flight campaigns, an amplitude correction using radiometric reference targets would be favorable (Höfle & Pfeifer, 2007).

The use of the trust-region algorithm shows a certain limitation of possible skewness values for echoes exceeding a width of 7 ns. We expect this dependency to be caused by the constraints introduced into the fitting algorithm. However, the number of echoes which are affected by this limitation (i.e. echoes with FHMW $>$ 7 ns and skewness $>$ 0.4) only accounts for 0.74% of the total number of fitted echoes. Therefore, we do not consider this as an issue.

2.5.2 Differences in tree species (RQ2)

Although there are some assumptions regarding the conceptual validity of fitting skewed functions to the waveform, we consider the found significant differences across the species to be robust.

The relevance of the energy and the amplitude of the *first*-echoes for species discrimination are in accordance with other studies. Although they used another waveform analysis approach, Hovi et al. (2016) reported the energy and the amplitude to be important features for species discrimination. Moreover, the applicability of the energy for species discrimination and classification has been demonstrated elsewhere (Reitberger et al., 2008; Heinzel & Koch, 2011).

Likewise, the applicability of the amplitude for tree species discrimination has been reported (e.g. Ørka et al., 2009; Hovi et al., 2016) and the FWHM, too, was demonstrated to show differences across species and to improve species classifications (Reitberger et al., 2008; Hollaus et al., 2009; Heinzel & Koch, 2011; Hovi et al., 2016).

However, considering discrimination potential of both the amplitude and the energy, we found that the species pairs which showed differences in the amplitude of the *first*-echoes are not the same subset as those for which we found differences in the energy.

In addition to the different significances of the echo attributes for tree species discrimination, the relevance of different return types becomes obvious. The two attributes which are directly related to the backscattered intensity, namely the echo amplitude and energy, show better performance using *first*-echoes only. This is not surprising, as first echoes are unaffected by previous scatterers (Korpela et al., 2012; Hovi et al., 2016). However, multiple returns could be corrected for attenuations (Richter et al., 2015), which would possibly increase the differences between the species in the respective attributes of *all*-echoes.

A third echo type that could be considered separately are only or single returns. Hovi et al. (2016) found these echoes to possess a high discrimination power in the energy attribute. However, as our implemented echo detection is rather sensitive, the number of only echoes is too small for a robust assessment (Tab. 2.3).

2.5.3 Potential causes for differences in the attributes

Previous studies have mainly focused on the influence of the properties of a single tree on the echo intensity. The intensity attribute was found to be affected by multiple factors as the mass, density and homogeneity of the foliage (Hollaus et al., 2009; Korpela et al., 2010; Hovi et al., 2016) on tree-level and by the leaf size, orientation and reflectivity on leaf-level (Korpela et al., 2010). Some of these factors again are controlled by tree health, age and height (Ørka et al., 2009; Korpela et al., 2010; Heinzel & Koch, 2011), as well as by stand characteristics and treatment (Hovi et al., 2016). Differences in these properties lead to intra-species variations of the attributes on tree-level.

On the other hand, as we discovered significant differences between species groups, we assume that generic properties for each species exist, leading to distinct, species specific signatures. The reported large overlap of some species in terms of echo attributes can likely be attributed to similar characteristics of foliage arrangement and crown shape.

2.5.3.1 Multiple scattering

Hovi & Korpela (2014) pointed out that for small-footprint laser scanners, the reflectance properties of the targets have a stronger influence on the backscattering than the actual structure of the targets. Hence, we suppose the skewness to be rather introduced by scattering effects, predominantly by higher order, volumetric scattering. The influence of higher order scattering for small-footprint laser scanner systems has been discussed before. Hovi & Korpela (2014) rated the contribution of first-order scattering to the total backscattering to be in the range of 57-88% only for small-footprint lasers while Morsdorf et al. (2009) mention a contribution of 86%, following the simulations by

Disney et al. (2006). Thus, multiple scattering may contribute to the total backscattering to a extent that can not be neglected entirely.

Multiple scattering is a known phenomenon which will impact the return waveform from large-footprint laser scanners (Sun & Ranson, 2000), tending to magnifying the return energy and leading to a slower decay of the reflected waveform (Kotchenova et al., 2003).

The scattering processes were found to be mainly controlled by leaf orientation and clumping on one hand (Ni-Meister et al., 2001; Romanczyk et al., 2013), and spectral reflectance, absorbance and transmittance properties of the target material in the wavelength of the laser on the other hand Disney et al. (2006). Furthermore, Hancock et al. (2012) stated that multiple scattering increases with increasing penetration depth, as more potential multiple scattering paths are available. Multiple scattering in vegetation is particularly evident in the near-infrared (1000-1500 nm) and this is as well the region, where most commercial ALS systems have their wavelength.

These findings are mainly derived from ray tracing approaches simulating medium to large-footprint systems. Nevertheless, some of the described effects coincide with the observations we made in this study. As shown in Fig. 2.12, the echo skewness for deciduous trees increases with decreasing height of the canopy layer. We attribute this to path modifications, i.e. range delays (Hancock et al., 2012), of the laser beam which are increasingly affected by multiple scattering.

The FWHM attribute was considered to contain information related to the structure of the targets, rather than to their optical properties (Heinzel & Koch, 2011). This implies that the FWHM mainly contains information about the extent and vertical distribution of the targets within the footprint (Jansa et al., 2007; Hovi et al., 2016). For extended targets (i.e. targets larger than the footprint size (Wagner et al., 2008a)), the local incidence angle was described to be the main factor driving FWHM differences (Wagner et al., 2008b). Hence, the FWHM is mainly caused by the vertical structure and the spatial arrangement of the leaves and branches in the case of small-footprint laser scanners (Heinzel & Koch, 2011). Evidence for this was provided by Persson et al. (2005) and Wagner et al. (2008a) who both found echoes deriving from vegetation to show larger FWHM values than those deriving from the terrain.

Consequently, multiple scattering is likely to also explain a certain amount of the detected variations in the FWHM (Hovi et al., 2016). The significant differences of the

FWHM between coniferous and deciduous tree species, which we partly ascribe to differences in the scattering properties of the crown types, are an indication for this assumption. Additional evidence is given by the increase of the echo width with increasing penetration depth into the crown, which increases the probability of higher order scattering (Hancock et al., 2012). However, the findings regarding decreasing FWHM for the bottom 30% of the crown do not fit that explanation and may indicate that additional processes may influence the FWHM, particularly in lower crown layers.

A final conclusion regarding the cause of the detected attribute variations and the influence of higher order scattering can not be made, at least based on our measurements, as the interactions of small-footprint laser with forest structure are complex and not yet fully understood (Romanczyk et al., 2013). Yet, we propose the echo skewness differences and parts of differences in the FWHM across the species to arise from differing multiple scattering effects of the species which result from differing crown properties regarding the distribution and the orientation of the leaves and the respective leaf optical properties. However, to broaden the understanding, more modelling as in the approaches by Disney et al. (2006),Morsdorf et al. (2009) or Hancock et al. (2012) is needed.

Further research should also comprise the sensor properties (Hovi & Korpela, 2014) and the acquisition geometry. These parameters were only roughly investigated.

2.5.3.2 Incidence angle

The incidence angle influences as well the echo amplitude and energy (Höfle & Pfeifer, 2007). The acquisition geometry is even more important in case of vegetation where the inclination angle of the leaves with respect to the laser alters the measured intensity (Hovi & Korpela, 2014). Hence, we expect this angle to influence the echo skewness to some degree, too.

To rate a possible bias on the measured echo skewness values introduced by the acquisition geometry, we correlated the scan angle to the skewness of the single, non-aggregated echoes. This showed only a very weak influence of the latter on the former, and we thus are considering the measurements to be unbiased in terms of incidence angle impacts.

2.5.3.3 Sensor properties

As depicted, the system waveform varies and is not of perfectly symmetric shape, but does not influence the skewness of the return echoes. However, further sensor parameters have to be considered. This particularly concerns the receiver impulse response, as this also affects the return waveform (Jutzi & Stilla, 2006a; Hovi et al., 2016). This comprises the sampling interval which is 1 ns for the used sensor and might alter the skewness of the waveform, introducing distortions in the feature extraction process (Hovi & Korpela, 2014). Such influences on the measured echo skewness were not further examined here. Possible approaches for further studies would be to introduce sensor models into ray tracing simulations (Hovi & Korpela, 2014).

2.5.3.4 Canopy structure

The plant area index (PAI) describing the canopy structure is a factor which possibly could explain some of the interaction processes of the laser beam with the canopy (Schneider et al., 2014), encompassing multiple scattering effects. For further investigations, the PAI and the structural complexity as described in (Leiterer et al., 2015) could be derived from ALS data and compared to our results.

In this context, we emphasize that we have no information about the plant species composing the understory of the test site as the tree map only reports the tree species at a given position. Although the number of returns decreases with decreasing height above ground, it is likely that other species from the understory also contribute to the detected waveform. This could distort the species specific signature in the analysed attributes.

2.5.4 Classification performance (RQ3)

As shown, the differentiation of coniferous and deciduous trees benefits from the additional echo attributes with an increase in terms of the overall accuracy and of Cohen's κ, respectively. However, the main improvement can be achieved by the two additional echo attributes of energy and FWHM, while the skewness and the kurtosis only lead to a minor improvement.

The classification accuracies for European beech are highest and show a clear increase in the producer's accuracy when the additional echo attributes are used. We relate this discrimination power for this species to the several echo attributes for which European beech differs significantly from the two other species (Tab. 2.6). However, as European beech dominates the training sample regarding the number of trees, we can not preclude a certain bias in the classification by the respective number of trees per species. Evidence for a certain bias is given by the low value of Cohen's κ and the high PA and UA of the dominating species which might be derived from the high per chance accuracy for this group.

On the other hand, the weak classification power for Sycamore maple and European ash, respectively, could be anticipated as the two species show nearly the same echo attribute signatures (Fig. 2.6).

A rigorous comparison of the classification power to other studies is difficult as other experiments vary regarding the number of tree samples, the number of tree species, and the study area. In addition, the data sets have different point densities (e.g. Yu et al., 2014; Heinzel & Koch, 2011). Additionally, the full-waveform features used in other studies differ from the ones used here (e.g. Hovi et al., 2016; Yu et al., 2014) and many of them deploy a more sophisticated set of general, point-cloud based structural features (e.g. Ørka et al., 2009; Vaughn et al., 2012; Li et al., 2013; Lindberg et al., 2014; Yu et al., 2014).

Regarding the overall accuracy and Cohen's κ alone, our classification power for coniferous and deciduous trees is in the same range as in Reitberger et al. (2008).

However, for the species classification, the mentioned studies reveal better classification performances in general. Our findings suggest that full-waveform ALS features alone might not be enough to provide an accurate tree species classifications in test sites such as ours.

2.5.4.1 Value of additional attributes

Although the species classification power merely showed a slight increase when additional attributes were added, we found that mainly the echo shape related parameters, i.e. the skewness and the kurtosis, were chosen as important attributes by the RF. This indicates a stronger prediction power in these attributes than in the amplitude attribute alone and furthermore indicates these attributes to comprise more information regarding the tree species than the energy related attributes. Hence, we claim a certain benefit of the additional echo attributes for the classification applications.

However, not always the attributes with the largest significant differences are the ones most relevant for the classification. As reported, the mean energy and the amplitude of the *first*-echoes showed the largest differences. However, of these two attributes, only the mean amplitude of the *first*-echoes was frequently selected among the ten most important attributes by the RF while the top three attributes all are related to the echo shape.

A possible explanation for this inconsistency between the two scores could be that in the RF, not only the number of differing species is important but the amount of variance between the species in the respective attributes, too, is considered. This variance was not accounted for in the simple count. Hence, the attribute importance as estimated by the RF might be more robust.

However, for more reliable assessments of the attribute importance, including a quantification of how much between-species variation is explained by each attribute, further studies should be undertaken. Additionally, we propose the use of these additional echo attributes for the fusion with data sets from other sensors (e.g. Torabzadeh et al., 2014)).

2.5.4.2 Challenges for operationalisation

As depicted in Fig. 2.6, the main drawbacks for the classification of the species solely based on aggregated echo attributes originate from the large intra-species variability and, related to this, from the huge overlap of the attribute value ranges between the species. Hence, despite significant differences in the echo attribute distributions across the species, the aggregated values characterising a single tree still are ambiguous to some extent, which weakens the discrimination power.

Hovi et al. (2016) reported that this large intra-species variations can mainly be attributed to the tree effect, that is, the inherent variations between the individual trees. This phenomenon was first described by Korpela et al. (2014) for the reflectances measured by a passive multispectral sensor. They found the same tree to appear in a similar way for all viewing directions. Furthermore, they proposed a stronger tree effect for sensor systems with constant backscattering geometries, as it is the case for LiDAR systems. Hence, we consider the aggregated echoes to reveal a robust measure of individual tree properties.

Finally, we only demonstrated the ability of the classification based on already delineated tree crowns. However, geometric errors in tree crown delineation might lead to shifts or uncertainties in the found attribute signatures of the species (Hovi et al., 2016).

2.6 Conclusion and outlook

In this study, we performed a waveform decomposition on FW ALS data using the skew normal distribution function (SND), for data from a temperate mixed forest. The SND allows us to model both symmetric and asymmetric echoes, and, compared to a standard Gaussian decomposition, which provides echo energy and width (FWHM), SND allows for the derivation of additional echo attributes, namely the skewness and kurtosis.

The examination of variations in the derived attributes across seven tree species illustrated the species to mainly differ in the energy and the amplitude of *first*-echoes and the skewness of *all*-echoes. When the attribute importance was assessed using RF, we found a clear shift of attribute importance towards the shape related echo attributes, i.e. the skewness and the kurtosis.

To show the benefit of the additional echo attributes, a differentiation of coniferous and deciduous trees and a species classification, respectively, were performed. The differentiation of coniferous and deciduous trees showed an improvement, if all attributes from the SND were used. Thus, for this task, waveform decomposition using the SND provides a certain benefit. On the other hand, the benefit for tree species classification is indistinct as this classification showed poor accuracies and a rather small improvement if only additional SND based FW attributes were added.

For operational applications, the FW features would need to be used alongside point-cloud based ALS feature sets or features derived from multispectral data.

For more reliable evidences regarding the benefit of the used FW features for species classification, the approach should be tested on a larger area comprising of a larger number of trees. Furthermore, we propose the integration of leaf-off data in addition to the leaf-on data. Reitberger et al. (2008) demonstrated leaf-off data to result in a better differentiation of coniferous and deciduous trees and Kim et al. (2009) could improve the differentiation with regard to the use of solely leaf-off and leaf-on data, respectively, if the two data sets were combined.

Besides, the classification could be refined if also decile aggregates of the attributes are used. However, the number of *first*-echoes decreases with the penetration depth into the crown what is likely to weaken the robustness of the respective attributes.

Although the majority of fitted echoes was of almost symmetric shape, turning the skewness signature of the trees weak when aggregated on crown level, we considered the differences across the species to be present. Further investigations regarding the propagation of the skewness values with increasing penetration depth into the crown revealed progress from slightly negative skewed echoes to symmetric or even positively skewed echoes. For the FWHM, we found a widening for lower layers. This behaviour was more distinct for deciduous than for coniferous species. We attribute these propagations mainly to multiple scattering effects.

As the computational cost of the SND is not larger than that of a normal Gaussian decomposition, the use of the additional features the SND provide (skewness and kurtosis) has no practical constraints and we encourage foresters to make use of these features in their classification frameworks. Given that our test site was a temperate mixed forest, the usefulness of these features in other forested ecosystems still needs to be tested.

However, the underlying physics causing the echo skewness through the interaction of the laser beam within the canopy are not fully understood and require further investigations. For this task, we propose ray tracing-based simulations, which also comprise sensor models. The latter would need close cooperation with instrument builders as Riegl and Optech. This would facilitate to study the impact of the sensor response on the waveform and potentially feedback design constraints to the sensor makers, such that FW data can be used to its fullest potential in tree species classification.

Furthermore, we suggest to investigate the echo skewness and its difference between the species under leaf-off conditions. Altered tree properties will affect the scattering, which should, according to our hypothesis, be visible in the echo shape.

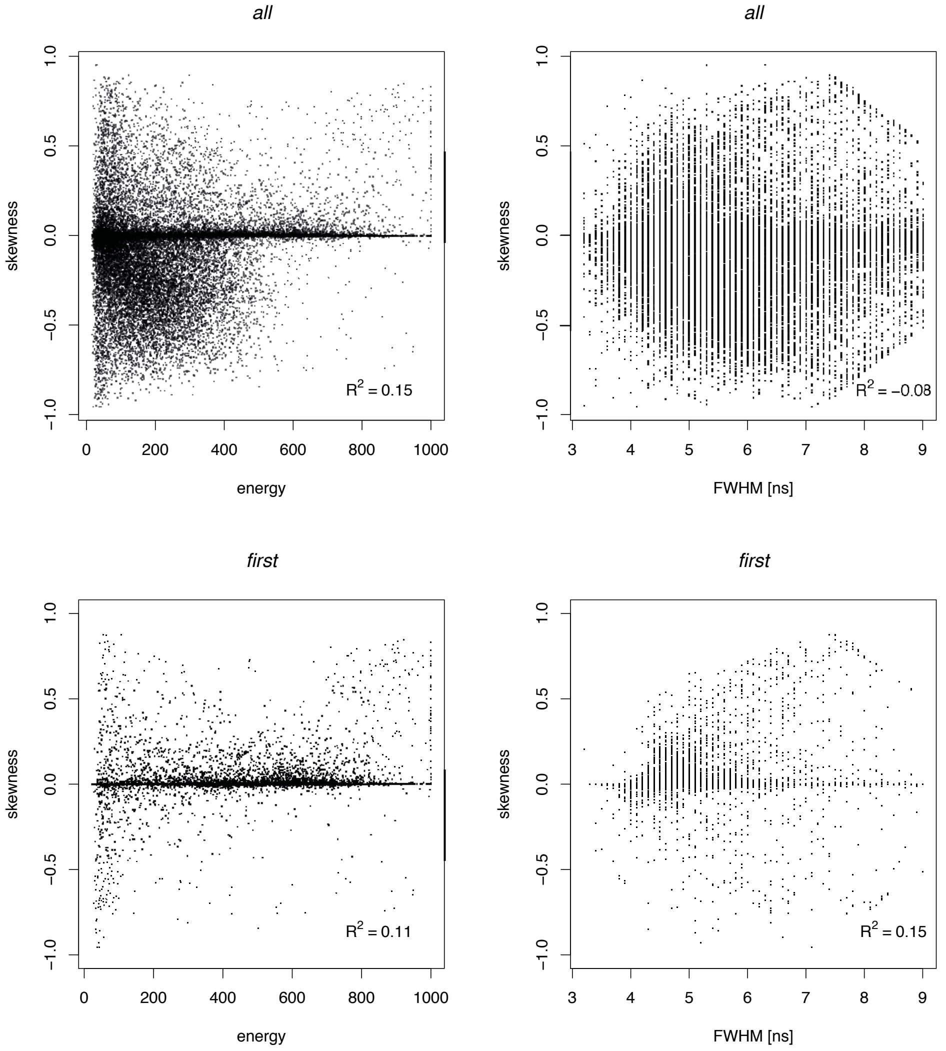

Figure 2.8.: Correlation between the echo skewness and echo energy and echo width, respectively. For a better demonstration, the plots show the echoes from 32 single European beech trees only, where the total number of echoes depicted in the plots is $N = 40'094$ for *all*-echoes and $N = 12'171$ for the *first*-echoes. The calculation of R^2 relates to the the entire set of crown echoes of all species types.

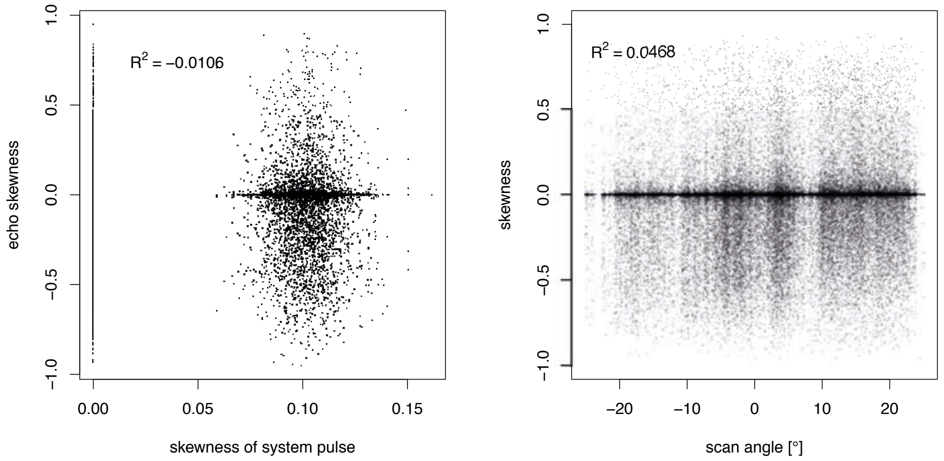

Figure 2.9.: Left: Correlation between the skewness of the system waveform and the echo skewness evaluated for $N = 13'452$ echoes originating from the canopies of European beech trees. Right: Correlation between the scan angle (off-nadir angle) and the skewness of the single echoes evaluated for the European beech trees comprising a total number of $N = 934'600$ crown echoes.

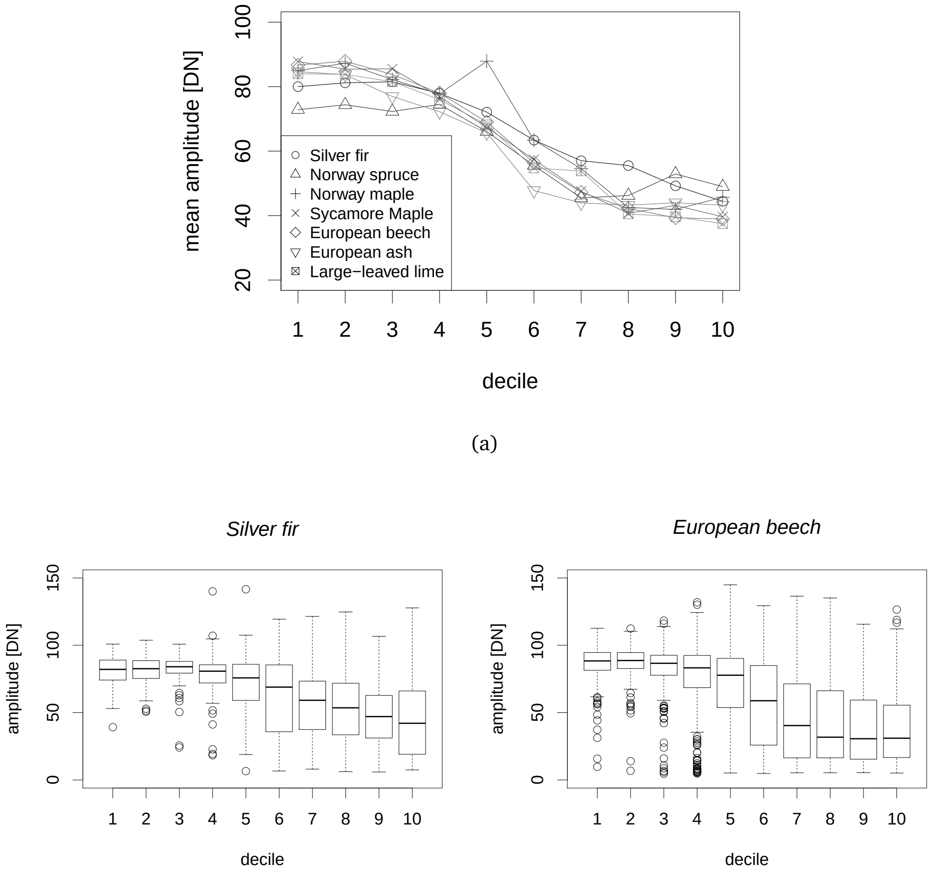

(a)

(b)

(c)

Figure 2.10.: a) Progression of the amplitude of the *first*-echoes (*first_A_mean_d#*, right) derived from the SND decomposition aggregated on decile level for each tree and averaged for each species. Further depicted are the amplitude ranges of *first*-echoes aggregated on decile level for the Silver fir trees (b) and the European beech trees (c). In the figures, 1 marks the top decile and 10 the bottom one.

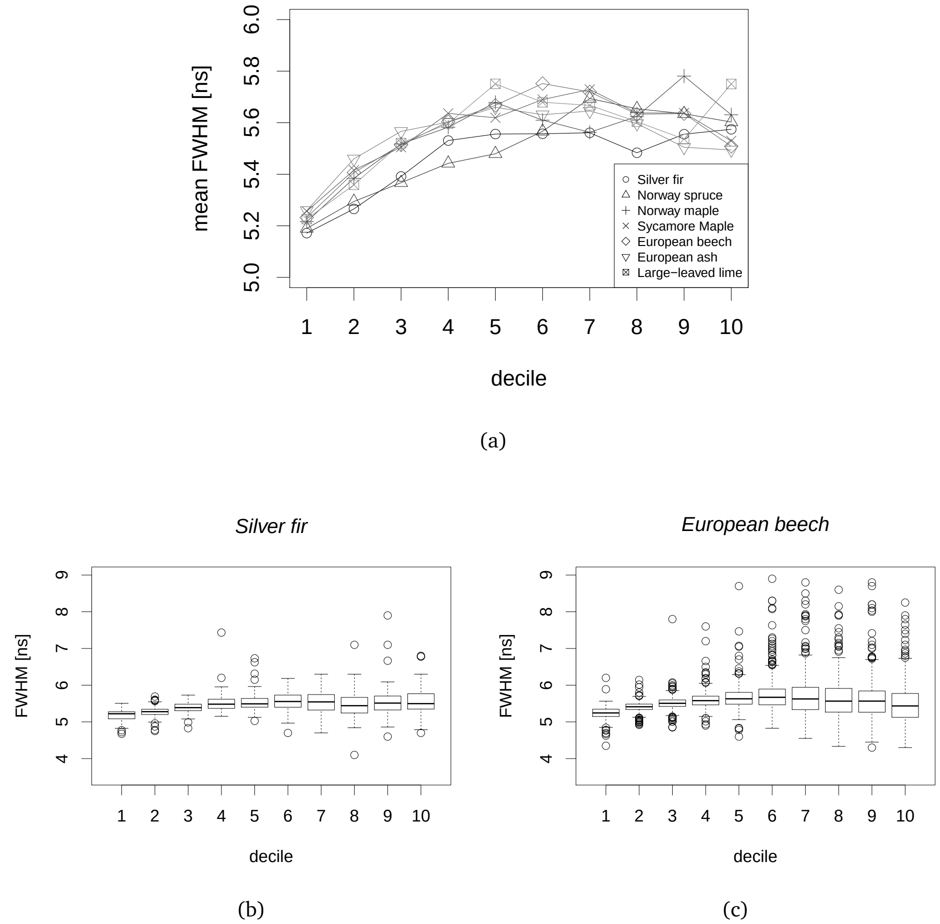

(a)

(b)

(c)

Figure 2.11.: a) Progression of the mean FWHM (*all_fwhm_mean_d#*) derived from the SND decomposition and aggregated on decile level for each tree and averaged for each species. Futher depicted are the FWHM ranges of *all*-echoes aggregated on decile level for the Silver fir trees (b) and the European beech trees (c). In the figures, 1 marks the top decile and 10 the bottom one.

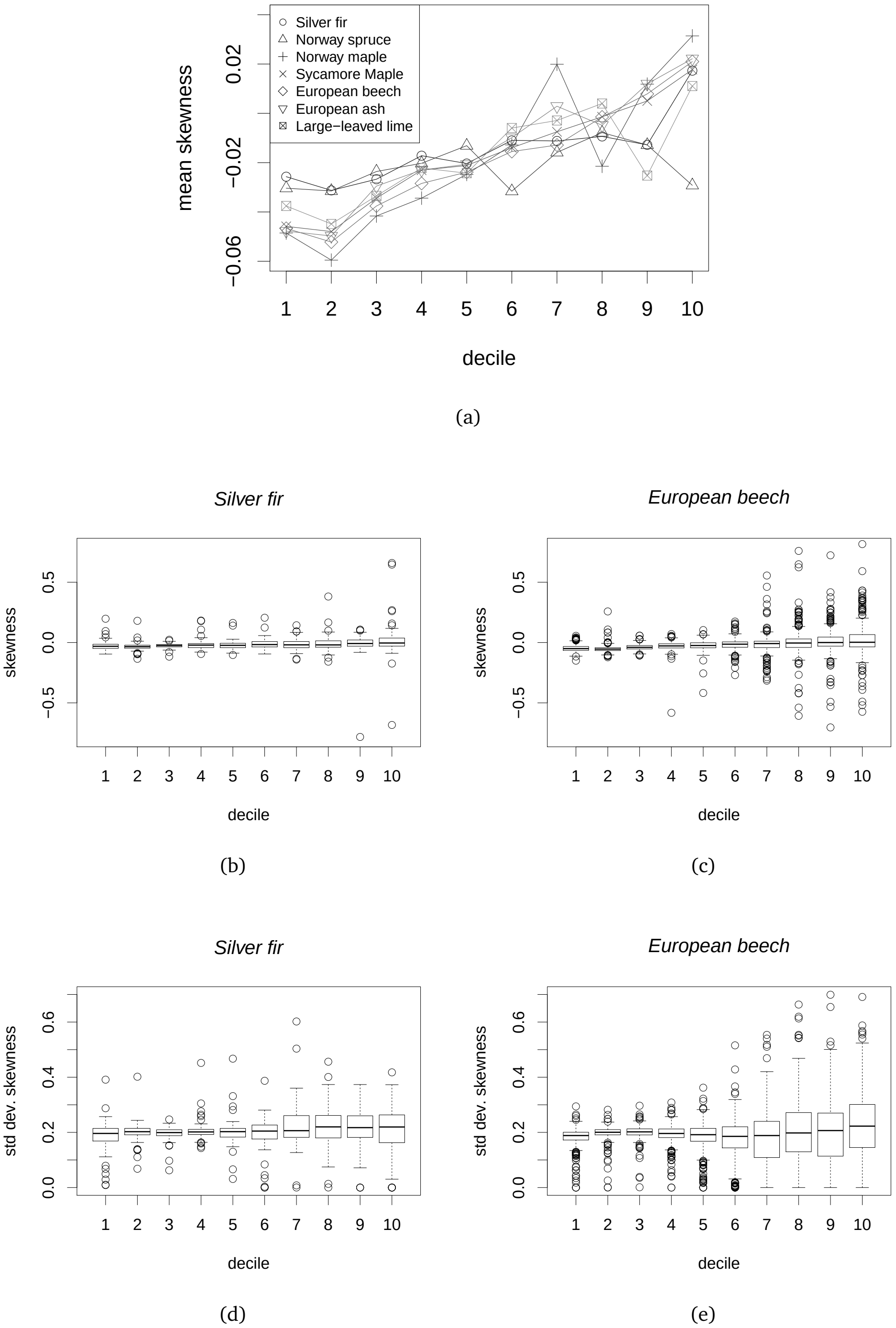

(a)

(b)

(c)

(d)

(e)

Figure 2.12.: a) Progression of the mean skewness (*all_skew_mean_d#*, left) aggregated on decile level for each tree and averaged for each species. Further shown are the skewness ranges of *all*-echoes aggregated on decile level for the Silver fir trees (b) and the European beech trees (c) as well as the ranges of the standard deviation of the skewness of *all*-echoes aggregated on decile level for Silver fir trees (d) and the European beech trees (e). In the figures, 1 marks the top decile and 10 the bottom one.

3 | Supplementary material

3.1 Rational of the approach

The hypothesis underlying our study was a possible skewness in the echoes which we wanted to detect, as stated in Chapter 2. We assume the skewness hypothesis to pertain to forested areas where we expect an influence of multiple scattering effects (Disney et al., 2006; Morsdorf et al., 2009; Hancock et al., 2012). Besides multiple scattering, Roncat (in review) presumes the geometry of the differential cross-section of the scatterers to contribute to the asymmetry in the return waveform, too. However, for our acquisition geometry comprising of a system pulse length of 4.5 ns and a footprint size of 25 cm, the shape of the return echoes is expected to be dominated by the shape of the system waveform. This corresponds to a Gaussian distribution for the LMS-Q680i (Fig. 3.7). Evidence for the strong influence of the system waveform can be found in simulations of return waveforms for different scatterer arrangements and geometries in Roncat (2014, p.139ff).

As the amount of impact of multiple scattering and the geometry, respectively, and the actual echo shape which can be expected were uncertain, we aimed at introducing as little constraints as possible into the curve fitting step. Hence, we seeked a parametric model for waveform decomposition, which enabled to model both, symmetric and asymmetric distributions, and comprised no limitations regarding the direction of the skewness. Finally, considering the shape of the system waveform, the model should additionally be derived from a Gaussian distribution.

Such a function was found in the skew normal distribution function (SND) introduced by Azzalini (1985). As mentioned in Section 2.3, the shape of the function is controlled by the shape parameter α and is of Gaussian shape for $\alpha = 0$, while a left skewness is achieved for $\alpha < 0$ and a right skewness for $\alpha > 0$ (Fig. 3.1).

On the other hand, we rejected other distribution functions proposed for waveform de-

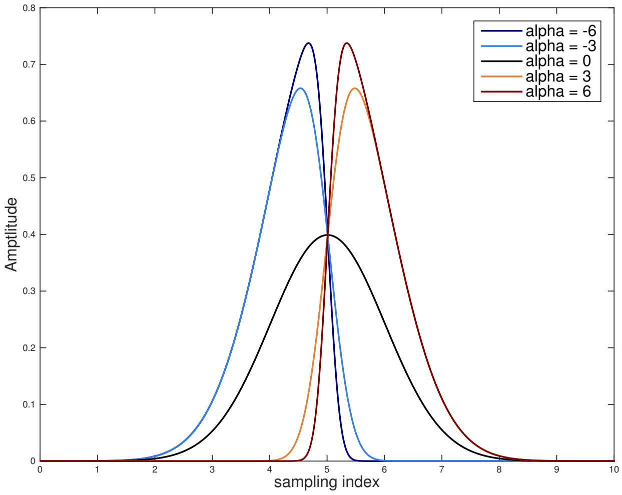

Figure 3.1.: Plot of the skew normal distribution function using different values for the shape parameter α. The plot illustrates the ability of the SND function to model left ($\alpha < 0$, blueish colors) and right skewed ($\alpha > 0$, reddish colors) distributions, respectively, as well as the symmetric normal distribution ($\alpha = 0$, black).

composition. We considered the Gaussian distribution (Hofton et al., 2000; Wagner et al., 2006) and the Generalized Gaussian distribution (Chauve et al., 2007) inappropriate for our task, as these functions are of symmetric shape. The Lognormal distribution (Chauve et al., 2007), the Burr distribution and the Nakagami distribution (Mallet et al., 2010) are able to model skewed distributions, but all of these functions are able to model right skewed distributions only. Furthermore, the two latter functions have no relation to the Gaussian distribution.

The deficiencies of the functions are exemplarily depicted for the Nakagami distribution.

3.1.1 Nakagami distribution

Mallet et al. (2010) introduced the Nakagami distribution for waveform decomposition in the framework of a reversible jump Markov chain Monte Carlo algorithm, where for each echo, the algorithm selects the most appropriate out of a set of possible functions. The Nakagami distribution is a generalized χ distribution and allows for the modelling of skewed echoes (Roncat, 2014). It is controlled by a shape parameter ξ and a spread parameter ω where the function is only defined for $\{\xi, \omega\} > 0$ (Wolfram, 2016). The formula was implemented as described in Mallet et al. (2010) as:

$$f(x|I,s,\xi,\omega) = I\frac{2\xi^{\xi}}{\omega\Gamma(\xi)}\left(\frac{x-s}{\omega}\right)^{2\xi-1} exp-\xi\left(\frac{x-s}{\omega}\right)^{2} \tag{3.1}$$

where x denotes the sample values of the waveform, I the amplitude and s the position of the distribution function on the time vector of x.

However, curve fitting evaluations of synthetic echoes illustrate the twofold deficiency of the Nakagami distribution for our research aim. Besides the mentioned restriction to right skewed distributions only, the evaluation reveals shortcomings in fitting a Gaussian shape. Fig. 3.2 compares the Nakagami to the SND decomposition for curve fitting of a synthetic echo. This is composed of two overlapping Gaussian distributions which form a left and a right skewed echo, respectively. The Nakagami distribution fits the right skewed echo (Fig. 3.2, bottom right) more appropriately than the left skewed (Fig. 3.2, top right) for which deviations from the actual echo over the entire signal length are revealed. This deviation originates from the inability of the Nakagami distribution to attain a left skewed shape. For the right skewed echo, the shape is modelled well around the maximum. Still, minor deviations occur in the lower parts of the signal, which emerge from the non-Gaussian origin of the Nakagami distribution.

The plots further reveal the strength of the SND decomposition, which copes well with modelling of both, left and right skewed echoes, and further fits well the lower parts of the echoes.

However, it has to be emphasized that the shortage of the Nakagami distribution to fit Gaussian shaped echoes only is an issue if we explicitly anticipate the respective principle shape based on the shape of the system waveform. The more important deficiency, which motivated us to reject the Nakagami distribution, was its inability to model left skewed to symmetric echoes.

3.2 Constraints for the trust-region algorithm

As proposed by Lin et al. (2010), the trust-region non-linear optimization algorithm introduced by Coleman & Li (1996) was used for waveform decomposition. The trust-region algorithm allows for constraining the parameter ranges of the function with which one aims to fit a given curve. This is an advantage over the Levenberg-Marquardt algorithm, which is often used for the decomposition (e.g. Hofton et al., 2000; Wagner et al.,

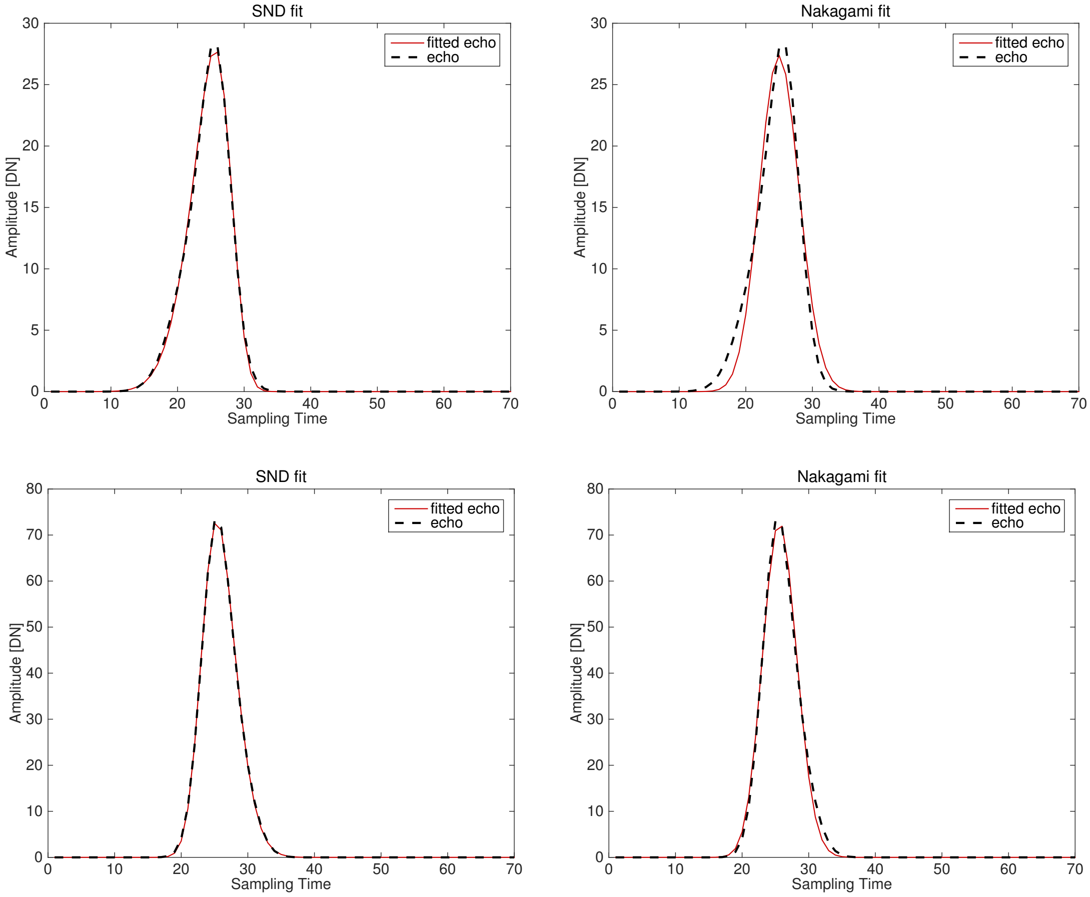

Figure 3.2.: Performance of the SND (left column) and the Nakagami decomposition (right column), respectively, for the modelling of a single, skewed echo. Depicted are the found solutions for the fit of a synthetic echo using a single distribution function. The synthetic echo is composed of two Gaussian distributions representing a left skewed (top row) and a right skewed (bottom row) echo, respectively.

2006).

By choosing appropriate constraints, the number of echoes violating the assumptions regarding valid attribute ranges and, hence, the number of echoes which have to be removed subsequently, can be reduced.

The primary goal was to constrain the maximum amplitude and the echo width of the fitted echoes, as well as to ensure the spacing between the echoes to be wide enough (Tab. 3.1). Reliable assumptions could be established for these echo attributes only, while we had no indications regarding valid attribute ranges for the echo skewness and kurtosis, respectively.

Table 3.1.: Assumed valid echo attribute ranges and the respective realization as constraints in the trust-region non-linear optimizer. FWHM_{sys} was choosen as 4.5 ns based on the analysis of the recorded system waveform. *previous* and *subsequent* in the first curve fitting iteration refer to the initial position of the previous and the subsequent echo, respectively, relative to the echo in question. Further information regarding the proper selection of echo attribute criterions can be found in Lin et al. (2010).

		lower limit	upper limit
echo attribute	amplitude	$>$ noise level	-
	spacing	resolution of system	
	FWHM	0.7FWHM_{sys}	2.0FWHM_{sys}
SND parameter	A	6	1000
	s	previous + 0.5FWHM_{sys}	subsequent + 0.5 FWHM_{sys}
	α	-10	10
	ω	0	6

While the skewness and the kurtosis attributes only depend on the shape parameter α (eq. 2.8; Fig. 3.3, bottom row), the FWHM results from the combination of α and the scale parameter ω (Fig. 3.3, top left). For the limits depicted in Tab. 3.1, the FWHM exceeds the defined maximum value of 9 ns for the combination of α values around zero and ω values near the upper limit. Hence, these values were eliminated (Fig. 3.3, top right). This echo removal step is reflected in the value ranges of α and ω found in the echoes from the actual waveform decomposition, where this gap in the distribution is clearly visible (Fig. 3.4, top right).

Fitting of echoes with too large echo widths could be avoided by defining narrower constraints for the parameters α and ω. Reasonably, in order to avoid too severe constraints for the echo skewness and kurtosis, only the constraints for the scale parameter ω should be modified. As depicted in Fig. 3.4 (top left), when choosing an upper limit of $\omega = 4.0$, the observed gap caused by the subsequent echo removal step could be avoided. This indicates that all fitted echoes over the entire range of α = [-10 10] show FWHMs narrower than 9 ns if the upper limit of ω is reduced.

Nonetheless, we found limitations in the skewness of the fitted echoes in dependence of increasing FWHM values exceeding a width of 5 ns (Fig. 3.4 bottom left) for the implementation with an upper limit of $\omega = 4.0$. For an upper limit of $\omega = 6.0$, the skewness limitation in dependence of the increasing FWHM only affected echoes exceeding a width of 7.0 ns (Fig. 3.4 bottom right).

Hence, a deficiency of the approach emerges in the trade-off between the limitation of the echo width and the independency of the echo skewness ranges of the FWHM.

As we intended to ensure as little dependency of the skewness of the FWHM as possible, we set the upper limit to $\omega = 6.0$, albeit an upper limit of $\omega = 4.0$ would have been the better choice from the perspective of the echo width criterion. We justify this larger upper limit by the anticipation that the majority of the fitted echoes is narrower than 9 ns. Evidence for this is given in Fig. 3.5 which illustrates a decrease in the number of echoes with increasing echo width. In consequence, even if the histogram shows the output of the decomposition pipeline with already eliminated echoes violating any of the made attribute assumptions, the total number of eliminated echoes can be assumed to be small. On the other hand, the impact of the FWHM on the skewness is reduced when using the higher upper limit.

3.3 Georeferencing

Apart from the decomposition, the georeferencing process is a crucial step in waveform processing. For ALS data, the localization of the echoes corresponds to a forward geocoding process as described in Lichti & Skaloud (2010). The time of flight of the laser to a scatterer in the known direction of the beam $\vec{d}$ is measured starting at the origin of the laser $\vec{o}$. This directly results in the position vectors $\vec{r_0}$, $\vec{r_1}$ of the scatterers at the ranges r_0, r_1 (Fig. 3.6). Hence, this approach requires all vectors to be in a cartesian coordinate system, which is the Universal Transverse Mercator (UTM) in our case, in order to enable the vector based calculation.

However, the approach for the given data set slightly differs from the principal approach described in Lichti & Skaloud (2010) and comprises of the following steps:

1. read the position of the laser's origin $\vec{o}$ and the direction vector $\vec{d}$ from the waveform file
2. translate the position vector of the origin $\vec{o}$ to cartesian coordinates in UTM
3. translate the direction vector $\vec{d}$ to cartesian coordinates in UTM
4. determine the echo position in UTM
5. translate the echo position from UTM to the local mapping frame CH1903 LV03

All necessary scripts for the translation were available at RSL. We focus on the principle steps in the description of the processing chain.

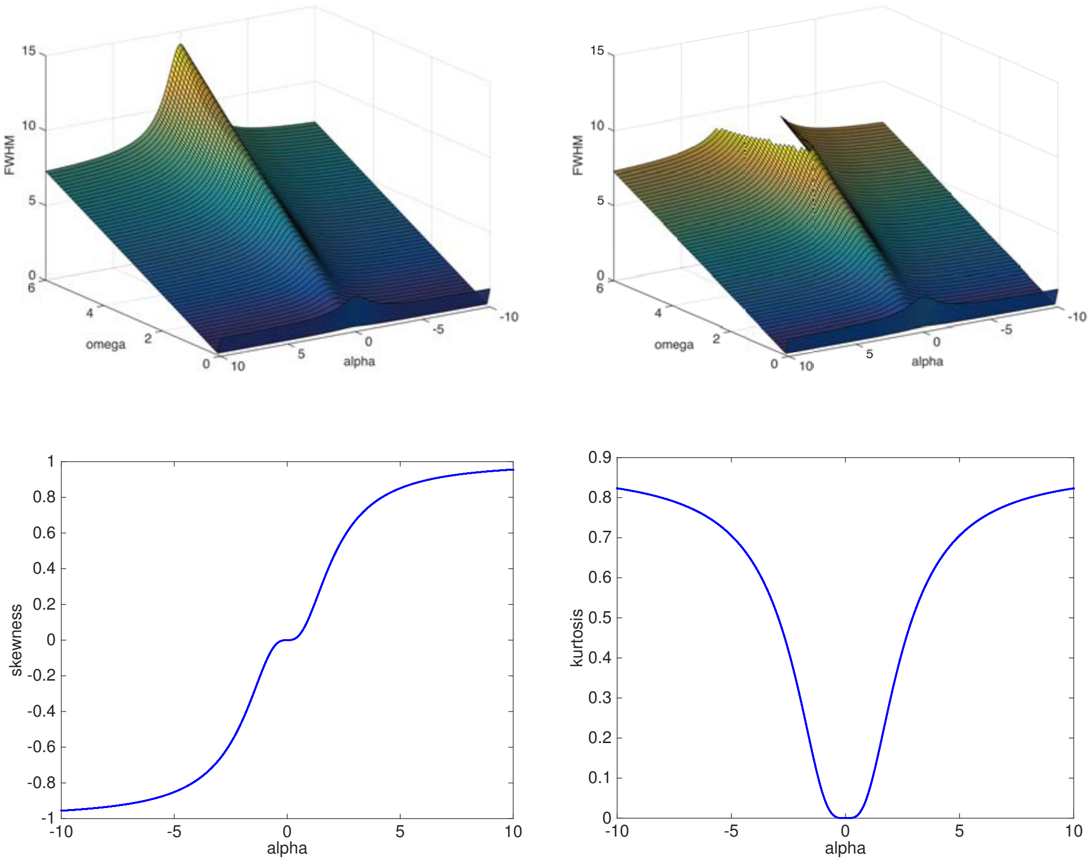

Figure 3.3.: Theoretical SND attribute ranges resulting from the introduced parameter constraints for α and ω depicted in Tab. 3.1. Top row: FWHM resulting from the combination of the parameters α and ω (left) and the subsequently removed FWHM values exceeding the defined upper limit of 9 ns (right). Bottom: relation between the shape parameter α and the skewness (left) and the kurtosis (right), respectively.

3.3.1 Translation of $\vec{o}$ into UTM

The position vector $\vec{o}$ of the origin of the laser and the direction vector $\vec{d}$ of the laser beam are stored in the waveform file in the s-frame, i.e. in the scanner's own coordinate system (socs). The rigorous approach for the translation from socs-coordinates into UTM would contain the translation of $\vec{o}$ from the s-frame into the earth centred-mapping frame (e-frame) via the body-frame of the carrier (b-frame). However, this process can be simplified when the flight trajectory information from the SBET (smoothed best estimate of trajectory), which stores the trajectory in WGS84 coordinates, and the timestamp of the pulse emission, i.e. the GPS-time, are used. Based on the GPS-time, the laser's origin $\vec{o}$ can directly be looked-up in the SBET. This is a feasible proceeding as the SBET stores the

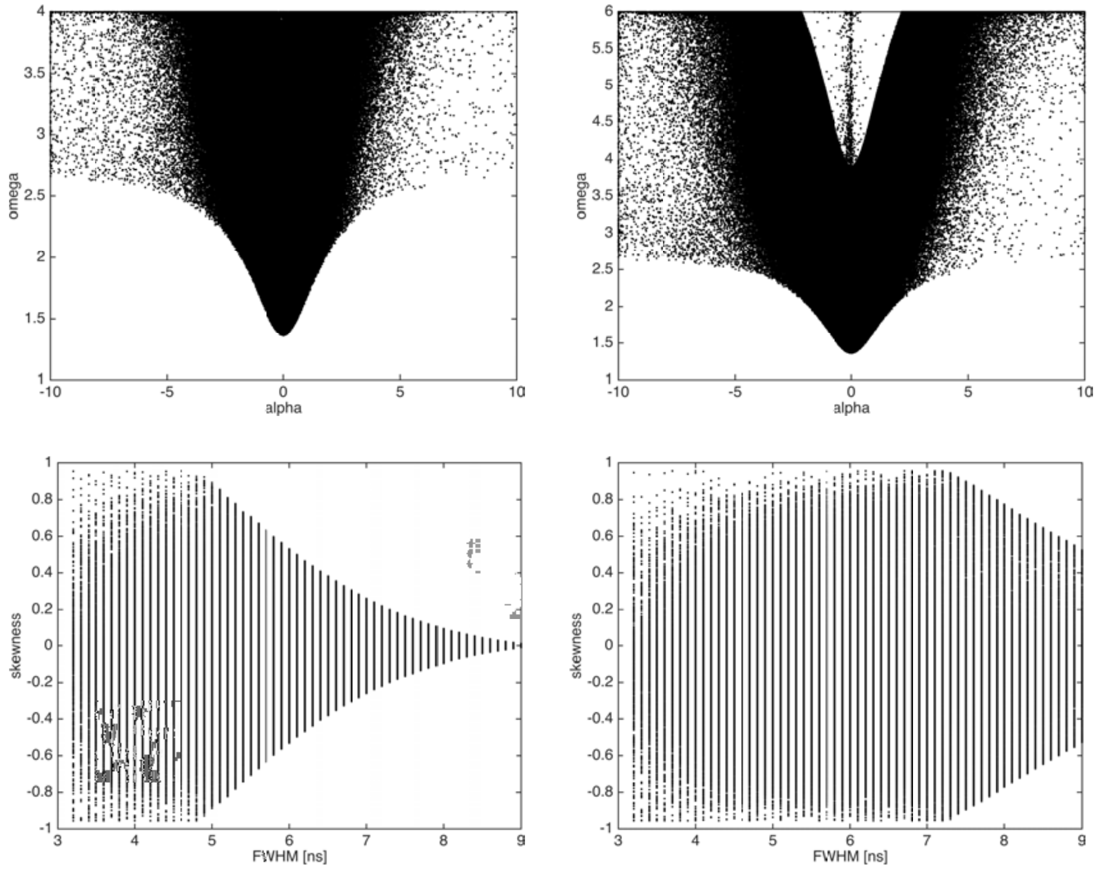

Figure 3.4.: SND parameter ranges for α and ω of the fitted echoes (top) and for the echo attributes FWHM and skewness (bottom), respectively. The figures depict the attribute values of all echoes present in the test site as found by the waveform decomposition after the echo removal step which eliminates echoes violating any attribute assumption. The results are achieved from the trust-region algorithm with an upper constraint of $\omega = 4.0$ (left) and an upper constraint of $\omega = 6.0$ (right), respectively, and α constrained to [-10 10].

position of the sensor's processing centre, which is equivalent to the origin of the laser, turning a boresight-correction redundant (personal communication, Stephan Landtwing, Swissphoto, Zurich, 15.10.2015). However, as the laser scanner was operated at a pulse repetition frequency of 200 kHz, while the SBET stores the position in a 200 Hz interval, the values in the SBET were linearly interpolated first. Subsequently, the position vector of the origin could be translated from ellipsoidal WGS84 coordinates into cartesian UTM coordinates.

The GPS-timestamp for each laser pulse, which corresponds to the reference time t_{ref} of the pulse, had to be determined to enable this simplified processing. However, this

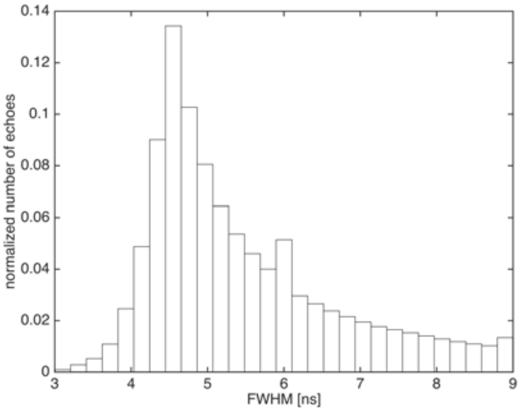

Figure 3.5.: FWHM distribution of all echoes present in the test site ($total = 8'983'263$ echoes) as fitted by the trust-region algorithm using the set of constraints depicted in Tab. 3.1 and after the elimination of echoes violating the attribute assumptions.

timestamp is not explicitly stored in the external GPS-time format in the waveform files and has to be calculated first (RIEGL, 2014). In order to determine t_{ref}, the index i had to be found where the system waveform reaches its maximum. Subsequently, the corresponding time could be calculated as external GPS-time using the equations stated in RIEGL (2014):

$$t_{sosbl_{external}} = t_{external} + (t_{sosbl} - t_{sorg}) \tag{3.2}$$

$$t_{i_{external}} = t_{sosbl_{external}} + i \cdot T_S \tag{3.3}$$

where t_{sorg} corresponds to the time instant when the sampling is started, t_{sosbl} to the start of the sampling block of the waveform, $t_{external}$ to the external time relative to the epoch and T_S to the sampling interval (1 ns for the LMS-Q series). All of these values are stored in the waveform file for each emitted pulse.

t_{ref} should be determined in sub-sampling-units for a rigorous georeferencing. As for the RIEGL LMS-Q560 (Wagner et al., 2006), we found the system waveform of the LMS-Q680i to be a Gaussian distribution. Thus, fitting a single Gaussian to the system waveform enabled the analytical determination of the index of the maximum (Fig. 3.7).

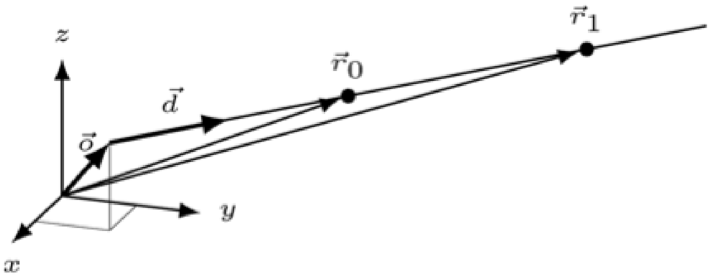

Figure 3.6.: The figure illustrates the principle of the forward georeferencing process. The range distance r_1 is determined based on the time of flight of the laser from the laser's origin $\vec{o}$ in beam direction $\vec{d}$. Walking along $\vec{d}$ for the range time results in the position vector of the scatterer $\vec{r_1}$ (RIEGL, 2014). However, all of these vectors as stored in the waveform file are in the scanner's own coordinate system, which makes the translation of the vectors into cartesian global coordinates necessary. (RIEGL, 2014).

3.3.2 Translation of $\vec{d}$ into UTM

As described for the position vector of the laser's origin $\vec{o}$, the direction vector $\vec{d}$ is already aligned in the b-frame, which is a right-handed frame (Lichti & Skaloud, 2010). Thus, the translation into UTM coordinates has to be done via the translation into the local-level l-NED frame (north-east-down oriented) using the compontents for $\vec{d}$ and the attitude of the platform which is stored in the SBET.

Using the available scripts written by Othmar Frey (Remote Sensing Laboratories, University of Zurich, Zurich, 2005), this step was straightforward.

3.3.3 Georeferencing of the echoes

Given the position vector of the laser's origin $\vec{o}$ and the direction vector $\vec{d}$ both in UTM, the position of an echo in UTM can be calculated based on the range r of target i where the range distance r_i is determined as (RIEGL, 2014):

$$r_i = \frac{v_g}{2}\left(t_i - t_{ref}\right) \tag{3.4}$$

where finally, the position of r_i in UTM can be determined as

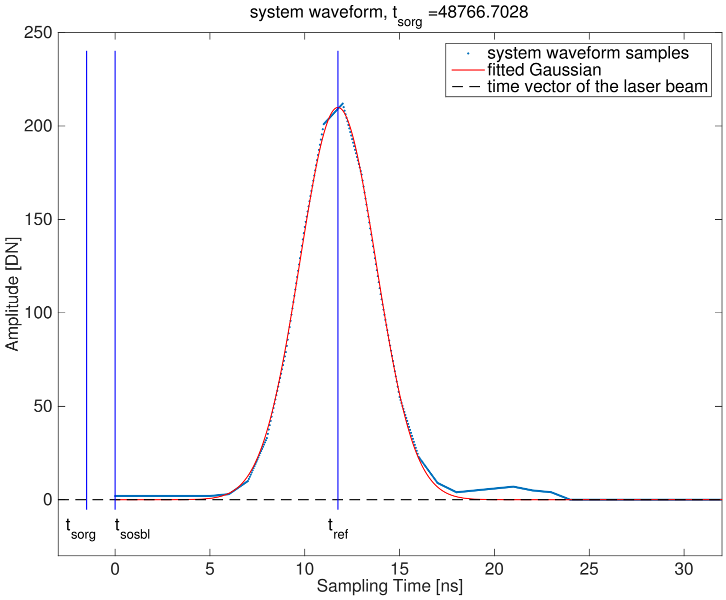

Figure 3.7.: Determination of the GPS-time by fitting a Gaussian distribution to the emitted laser pulse which is stored in the waveform file. t_{ref} corresponds to the instant where the emitted pulse reaches its maximum. Further depicted are the timestamps t_{sorg} and t_{sosbl}, respectively, which are important for the calculation and which are stored for every laser pulse.

$$\vec{r_i}_{UTM} = \vec{o}_{UTM} + \vec{d}_{UTM} r_i \tag{3.5}$$

In the formula above, v_g corresponds to the group velocity of light and t_i is the time in the external time format at which the echo is scattered back to the sensor. It is calculated the same way as t_{ref} using eq. 3.2 and eq. 3.3 where i in this case is the time instant where the echo reaches its maximum. This corresponds to the position of the echo on the waveform and is one of four output parameters provided by the waveform decomposition pipeline as implemented by us.

The final step for the georeferencing was the transformation of the coordinates from UTM to the local mapping frame which was CH1903 LV03 in this study.

3.3.4 Inconsistencies in the start of sample block time

As depicted in eq. 3.2, the start of sample block time t_{sosbl} plays a major role in the entire georeferencing process. This timestamp marks the time instant of the first sample of the waveform and, hence, is unique for every waveform sample (RIEGL, 2014). Furthermore, t_{sosbl} of the sampled return waveform differs from t_{sosbl} of the associated system pulse as the recording of the return waveform only starts in presence of a backscattered signal and, thus, is delayed relative to the emitted pulse. Consequently, $t_{sosbl,St}$ of the system waveform must necessarily precede $t_{sosbl,Pt}$ of the return waveform.

However, we found this prerequisite violated in the transition zone of the mirror facets of the sensor. In these zones, the difference $t_{sosbl,Pt} - t_{sosbl,St}$ becomes negative (Fig. 3.8, top). According to Andreas Roncat (TU Vienna, personal communication, 3.11.2015), the problem can be understood as unintended multiple times around (MTA) where at the end of a scan line, the return waveform is appended to the subsequent system pulse.

The issue can be solved by shifting the waveform back to the previous system pulse in case the term $t_{sosbl,Pt} - t_{sosbl,St}$ is negative (Andreas Roncat, TU Vienna, personal communication, 3.11.2015). However, this procedure is only valid if the incorrectly stored return waveform originates from the same mirror facet as the previous system pulse, that is, shifting is allowed within the same MTA-zone only. Thus, this criterion was checked before shifting and in case the criterion was violated, the respective return waveform was deleted.

3.3.5 Strip adjustment

No rigorous strip adjustment was performed as the task of this thesis was the gain of echo parameters for echoes originating from tree crowns based on waveform decomposition. To fulfill this task, a position accuracy in the range of 10^{-2} m is sufficient. However, in order to minimize positioning shifts present between point cloud tiles extracted from different flight strips, the single tiles covering the test site were adjusted using the iterative closest point (ICP) method. As reference for the alignment, we used a point cloud processed from the same data set, which was georeferenced by the data provider. The ICP was performed using *icp2.m* which is a MATLAB implementation by Mian (2005). The tolerance distance, within which closest points are searched, was set to 2 m.

For the 43 tiles into which the test site was split up for the decomposition, 39 tiles could be aligned with the ICP algorithm. The mean error after the ICP for these 39 files was 29.67 cm (Fig. 3.9). As illustrated in Fig. 3.10, the point clouds could be well aligned using the ICP correction, what subsequently allowed for a reliable extraction of single trees.

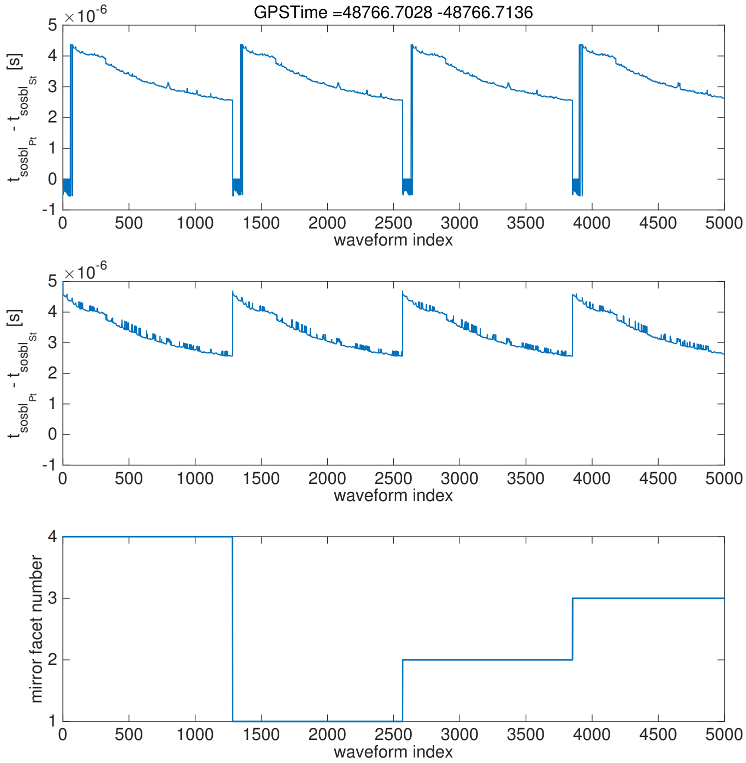

Figure 3.8.: For the LMS-Q680i, the return pulses are appended to the wrong system pulses at the transitions of the mirror facets (bottom). This leads to negative differences between $t_{sosbl,Pt}$ and $t_{sosbl,St}$ (top), which would mean that the return waveform precedes the system pulse. Shifting the affected return waveform back to the immediately previous system pulse eliminates the issue of negative time differences (middle).

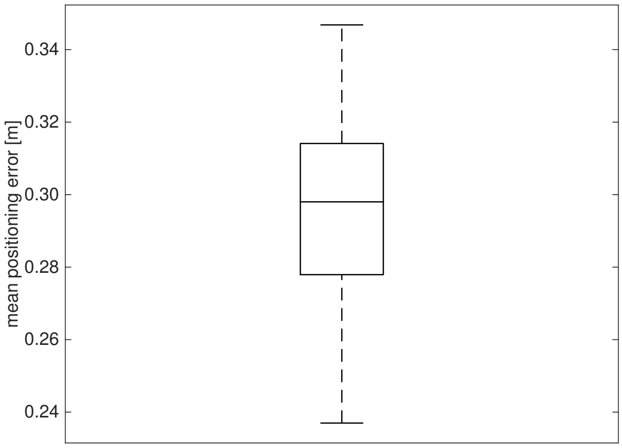

Figure 3.9.: Range of the mean error in the alignment per tile for a total of 39 point cloud tiles using the iterative closest point algorithm.

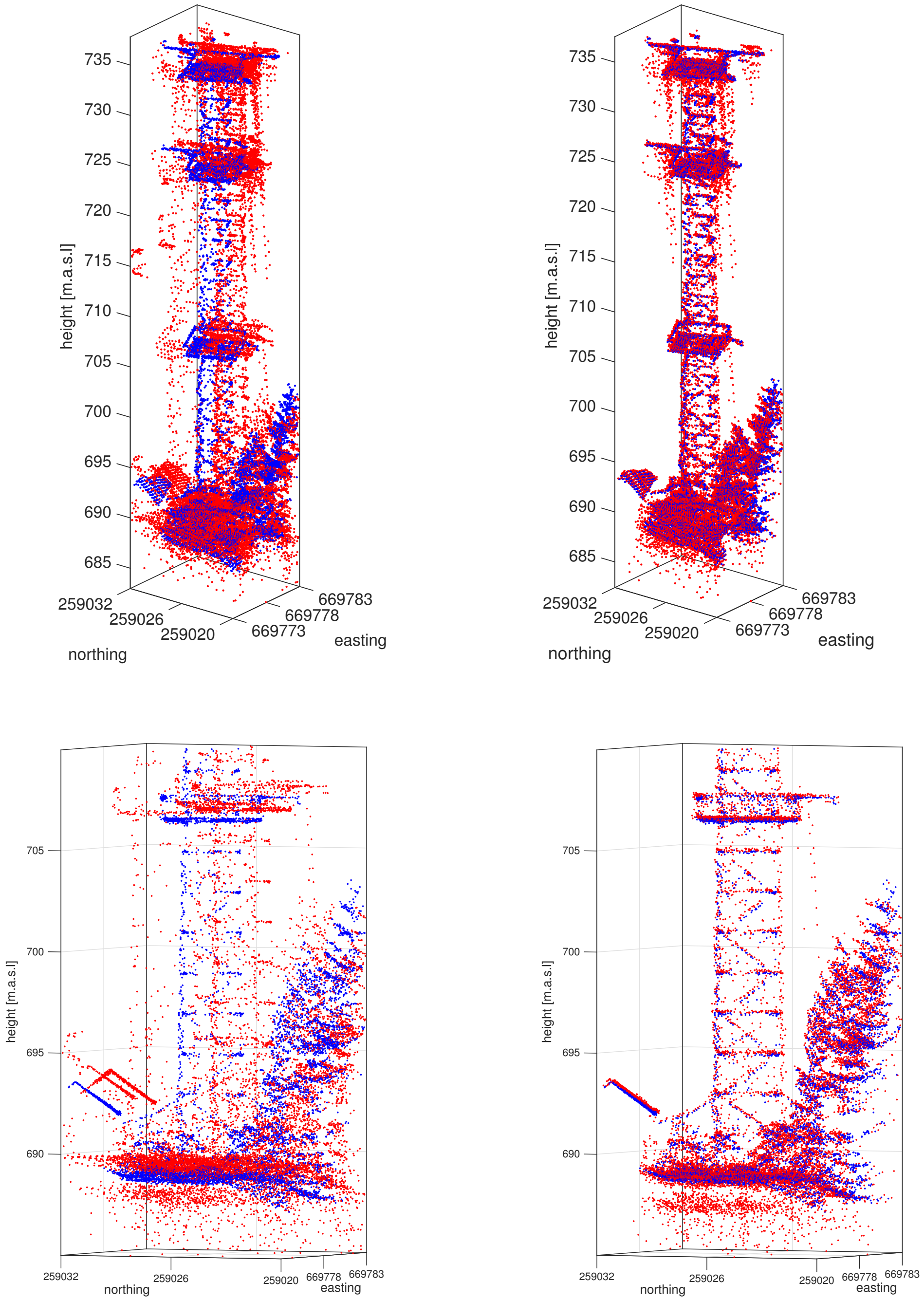

Figure 3.10.: Subset of the point cloud resulting from the implemented decomposition showing a flux tower and a roof, respectively, present in the test site. Depicted are the point cloud from the SND decomposition (red) and the georeferenced point cloud provided by the data vendor (blue), which was used as reference for the alignment. Top, left: non-adjusted SND decomposition, illustrating a shift between the two point clouds. Top, right: SND decomposition with ICP alignment performed on the data set. Bottom: Detail of the subset showing the improvement in the alignment in the area of the roof. The aligned point cloud tiles (right) show a clear improvement in the georeferencing compared to the point clouds without alignment (left).

4 | Synthesis

The skew normal distribution (SND) enhances the set of parametric functions proposed for the decomposition of the return waveform from small-footprint laser scanners, whereby the applicability of the SND for this task could be attested in our study. The SND is a very flexible parametric model which allows for the fitting of symmetric, normally distributed echoes. Furthermore, it is able to model a potential skewness of the echoes. The advantage of the SND lies in the opportunity to retrieve all echo features provided by the Gaussian distribution. But additionally, the third and fourth statistical moments, i.e. the echo skewness and kurtosis, can be analysed whereas no anticipations regarding the direction of the skewness are introduced. This is in contrast to all other parametric functions proposed for waveform decomposition, which allow for the modelling of skewed echoes but introduce a presupposition regarding the direction of the skewness.

The focus of our study rested on the application of full-waveform ALS data for tree species classification. The aim was the investigation of across species differences in the echo attributes derived from the SND decomposition. Besides differences present in the echo amplitude, energy and width, which were described in previous studies (e.g. Reitberger et al., 2008; Heinzel & Koch, 2011; Hovi et al., 2016), we found significant differences between the tree species in the additional echo attributes provided by the SND, particularly in the echo skewness. This indicates a benefit of the additional attributes for species classification and, thus, the use of the SND for waveform decomposition. The benefit of the SND attributes could be demonstrated for the differentiation of coniferous and deciduous trees. For species classification, we propose the use of the full-waveform features as derived in this study in combination with features derived from multispectral data. The main issues for the species classification based on the full-waveform features are the large within-species variations of the features and the huge overlap of the feature ranges across the species.

However, performing waveform decomposition is not the only possible approach when aiming at describing higher order statistical moments. We suggest that the approaches, which perform the analysis directly on the waveform (e.g. Yu et al., 2014; Hovi et al., 2016), could be extended by the calculation of the skewness and the kurtosis. Moreover, Roncat (in review) demonstrated that these attributes can be retrieved based on a B-splines deconvolution approach, too. However, in contrast to our study describing the echoes, the latter approach focuses on the targets (Roncat et al., 2011; Roncat, in review), hence, the attributes have a different physical meaning.

We suppose the detected echo skewness to be caused by multiple scattering mainly for which we found some indications, whereas the impact of the geometry of the scatterers was not investigated. We propose to further examine the interactions of small-footprint laser with tree crowns based on ray tracing simulations to improve the understanding of the factors causing the echo skewness. An improved comprehension of the physical causes and meaning of the skewness will subserve the interpretation of the measurements and enable a proper incorporation of the shape related echo attributes into existing classification frameworks.

References

Armston, J., Disney, M., Lewis, P., Scarth, P., Phinn, S., Lucas, R., Bunting, P., & Goodwin, N. (2013). Direct retrieval of canopy gap probability using airborne waveform lidar. *Remote Sensing of Environment*, *134*, 24 – 38.

Azzalini, A. (1985). A class of distributions which includes the normal ones. *Scandinavian Journal of Statistics*, *12*, 171–178.

Baltsavias, E. P. (1999). Airborne laser scanning: basic relations and formulas. *ISPRS Journal Of Photogrammetry And Remote Sensing*, *54*, 199–214.

Blair, J., & Hofton, M. (1999). Modeling laser altimeter return waveforms over complex vegetation using high-resolution elevation data. *Geophysical Research Letters*, *26*, 2509–2512.

Brandtberg, T. (2007). Classifying individual tree species under leaf-off and leaf-on conditions using airborne lidar. *ISPRS Journal of Photogrammetry and Remote Sensing*, *61*, 325–340.

Breiman, L. (2001). Random forests. *Machine Learning*, *45*, 5–32.

Chang, C.-C., & Lin, C.-J. (2011). Libsvm: A library for support vector machines. retrieved from: http://www.csie.ntu.edu.tw/ cjlin/libsvm/. (16.3.2016).

Chauve, A., Mallet, C., Bretar, F., Durrieu, S., Pierrot Deseilligny, M., & Puech, W. (2007). Processing full-waveform lidar data: Modelling raw signals. *IAPRS International Archives of Photogrammetry, Remote Sensing and Spatial Information Sciences*, *36*, 102–107.

Coleman, T., & Li, Y. (1996). An interior trust region approach for nonlinear minimization subject to bounds. *SIAM Journal on Optimization*, *6*, 418–445.

Disney, M., Lewis, P., & Saich, P. (2006). 3d modelling of forest canopy structure for remote sensing simulations in the optical and microwave domains. *Remote Sensing of Environment*, *100*, 114–132.

Eugster, W., Zeyer, K., Zeeman, M., Michna, P., Zingg, A., Buchmann, N., & Emmenegger, L. (2007). Methodical study of nitrous oxide eddy covariance measurements using quantum cascade laser spectrometery over a Swiss forest. *Biogeosciences*, *4*, 927–939.

FAO (2010). *Global Forest Resources Assessment 2010. Main report. FAO Forestry Paper No. 163.* Food and Agriculture Organization of the United Nations, Rome, Italy.

Hancock, S., Lewis, P., Foster, M., Disney, M., & Muller, J.-P. (2012). Measuring forests with dual wavelength lidar: A simulation study over topography. *Agricultural and Forest Meteorology*, *161*, 123–133.

Heinzel, J., & Koch, B. (2011). Exploring full-waveform lidar parameters for tree species classification. *International Journal of Applied Earth Observation and Geoinformation*, *13*, 152 – 160.

Höfle, B., & Pfeifer, N. (2007). Correction of laser scanning intensity data: Data and model-driven approaches. *ISPRS Journal Of Photogrammetry And Remote Sensing*, *62*, 415–433.

Hofton, M. A., Minster, J. B., & Blair, J. B. (2000). Decomposition of laser altimeter waveforms. *IEEE Transactions on Geoscience and Remote Sensing*, *38*, 1989–1996.

Hollaus, M., Mücke, W., Höfle, B., Dorigo, W., Pfeifer, N., Wagner, W., Bauerhansl, C., & Regner, B. (2009). Tree species classification based on full-waveform airborne laser scanning data. *Proceedings of SILVILASER*, (pp. 54–62).

Holmgren, J., & Persson, A. (2004). Identifying species of individual trees using airborne laser scanner. *Remote Sensing Of Environment*, *90*, 415–423.

Hovi, A., Korhonen, L., Vauhkonen, J., & Korpela, I. (2016). LiDAR waveform features for tree species classification and their sensitivity to tree- and acquisition related parameters. *Remote Sensing Of Environment*, *173*, 224–237.

Hovi, A., & Korpela, I. (2014). Real and simulated waveform-recording lidar data in juvenile boreal forest vegetation. *Remote Sensing of Environment*, *140*, 665–678.

Hyyppä, J., Hyyppä, H., Leckie, D., Gougeon, F., Yu, X., & Maltamo, M. (2008). Review of methods of small-footprint airborne laser scanning for extracting forest inventory data in boreal forests. *International Journal Of Remote Sensing*, *29*, 1339–1366.

Jansa, J., Wagner, W., & Melzer, T. (2007). Die Arbeiten im Christian-Doppler-Labor für Räumliche Daten aus Laserscanning und Fernerkundung. In *Strobl, J., Blaschke, T., Griesebner, G. (Eds.), Angewandte Geoinformatik 2007. Beiträge zum 19. AGIT Symposium Salzburg*. Wichmann Verlag, Heidelberg, Germany. 912 pages.

Jörg, P. C., Weyermann, J., Morsdorf, F., Zemp, M., & Schaepman, M. E. (2015). Computation of a distributed glacier surface albedo proxy using airborne laser scanning intensity data and in-situ spectro-radiometric measurements. *Remote Sensing Of Environment*, *160*, 31–42.

Jutzi, B., & Stilla, U. (2006a). Characteristics of the measurement unit of a full-waveform laser system. *Revue Francaise de Photogrammetrie et de Teledetection*, (pp. 17–22).

Jutzi, B., & Stilla, U. (2006b). Range determination with waveform recording laser systems using a Wiener Filter. *ISPRS Journal Of Photogrammetry And Remote Sensing*, *61*, 95–107.

Kangas, A., Gove, J. H., & Scott, C. T. (2006). Introduction. In A. Kangas, & M. Maltamo (Eds.), *Forest Inventory* (pp. 3–11). Springer, The Netherlands.

Kim, S., McGaughey, R., Andersen, H.-E., & Schreuder, G. (2009). Tree species differentiation using intensity data derived from leaf-on and leaf-off airborne laser scanner data. *Remote Sensing of Environment*, *113*, 1575–1586.

Koetz, B., Morsdorf, F., van der Linden, S., Curt, T., & Allgoewer, B. (2008). Multi-source land cover classification for forest fire management based on imaging spectrometry and LiDAR data. *Forest Ecology and Management*, *256*, 263–271.

Koetz, B., Morsdorf, F., Sun, G., Ranson, K., Itten, K., & Allgower, B. (2006). Inversion of a lidar waveform model for forest biophysical parameter estimation. *IEEE Geoscience and Remote Sensing Letters*, *3*, 49–53.

Korpela, I., Hovi, A., & Morsdorf, F. (2012). Understory trees in airborne LiDAR data - Selective mapping due to transmission losses and echo-triggering mechanisms. *Remote Sensing Of Environment*, *119*, 92–104.

Korpela, I., Mehtätalo, L., Markelin, L., Seppänen, A., & Kangas, A. (2014). Tree species identification in aerial image data using directional reflectance signatures. *Silva Fennica*, *48*, 1–20.

Korpela, I., Ørka, H. O., Maltamo, M., Tokola, T., & Hyyppa, J. (2010). Tree Species Classification Using Airborne LiDAR - Effects of Stand and Tree Parameters, Downsizing of Training Set, Intensity Normalization, and Sensor Type. *Silva Fennica*, *44*, 319–339.

Kotchenova, S., Shabanov, N., Knyazikhin, Y., Davis, A., Dubayah, R., & Myneni, R. (2003). Modeling lidar waveforms with time-dependent stochastic radiative transfer theory for remote estimations of forest structure. *Journal of Geophysical Research D: Atmospheres*, *108*, ACL 12–1 – ACL 12–13.

Lefsky, M., Cohen, W., Acker, S., Parker, G., Spies, T., & Harding, D. (1999). Lidar remote sensing of the canopy structure and biophysical properties of douglas-fir western hemlock forests. *Remote Sensing of Environment*, *70*, 339–361.

Leiterer, R., Torabzadeh, H., Furrer, R., Schaepman, M. E., & Morsdorf, F. (2015). Towards Automated Characterization of Canopy Layering in Mixed Temperate Forests Using Airborne Laser Scanning. *Forests*, *6*, 4146–4167.

Li, J., Hu, B., & Noland, T. (2013). Classification of tree species based on structural features derived from high density lidar data. *Agricultural and Forest Meteorology*, *171-172*, 104–114.

Lichti, D., & Skaloud, J. (2010). Registration and calibration. In G. Vosselman, & H.-G. Maas (Eds.), *Airborne and Terrestrial Laser Scanning* (pp. 83–133). Whittles Publishing, Dunbeath, Scotland, UK. 320pp.

Lin, Y.-C., Mills, J. P., & Smith-Voysey, S. (2010). Rigorous pulse detection from full-waveform airborne laser scanning data. *International Journal Of Remote Sensing*, *31*, 1303–1324.

Lindberg, E., Eysn, L., Hollaus, M., Holmgren, J., & Pfeifer, N. (2014). Delineation of tree crowns and tree species classification from full-waveform airborne laser scanning data using 3-d ellipsoidal clustering. *IEEE Journal of Selected Topics in Applied Earth Observations and Remote Sensing*, *7*, 3174–3181.

Lu, D. (2006). The potential and challenge of remote sensing-based biomass estimation. *International Journal of Remote Sensing*, *27*, 1297–1328.

Malenovský, Z., Mishra, K. B., Zemek, F., Rascher, U., & Nedbal, L. (2009). Scientific and technical challenges in remote sensing of plant canopy reflectance and fluorescence. *Journal of Experimental Botany*, *60*, 2987–3004.

Mallet, C. (2010). *Analyse de données lidar à Retour d'Onde Complète pour la classication en milieu urbain*. Ph.D. thesis École Doctorale d'Informatique, Télécommunications et Électronique de Paris, Télécom ParisTech, Paris.

Mallet, C., & Bretar, F. (2009). Full-waveform topographic lidar: State-of-the-art. *ISPRS Journal Of Photogrammetry And Remote Sensing*, *64*, 1–16.

Mallet, C., Lafarge, F., Roux, M., Soergel, U., Bretar, F., & Heipke, C. (2010). A marked point process for modeling lidar waveforms. *IEEE Transactions on Image Processing*, *19*, 3204–3221.

MathWorks (2016a). Documentation, lsqcuvefit. The MathWorks, Inc., Natick, MA. Retrieved from: http://ch.mathworks.com/help/optim/ug/lsqcurvefit.html. (16.1.2016).

MathWorks (2016b). Normal Distribution. The MathWorks, Inc. Natick, MA. Retrieved from: http://ch.mathworks.com/help/stats/normal-distribution.html. (13.3.2016).

MATLAB (2014). MATLAB 8.4, The MathWorks Inc., Natick, MA.

Melgani, F., & Bruzzone, L. (2004). Classification of hyperspectral remote sensing images with support vector machines. *IEEE Transactions on Geoscience and Remote Sensing*, *42*, 1778–1790.

Mian, A. S. (2005). Iterative Closest Point algorithm. icp2.m. School of Computer Science and Software Engineering, The University of Western Australia, Crawley, Australia. Retrieved from: https://searchcode.com/codesearch/view/13619753/. (13.6.2016).

Millennium Ecosystem Assessment (2005). *Ecosystems and Human Well-being: Biodiversity Synthesis*. World Resources Institute, Washington DC.

Morsdorf, F., Mårell, A., Koetz, B., Cassagne, N., Pimont, F., Rigolot, E., & Allgöwer, B. (2010). Discrimination of vegetation strata in a multi-layered mediterranean forest ecosystem using height and intensity information derived from airborne laser scanning. *Remote Sensing of Environment*, *114*, 1403–1415.

Morsdorf, F., Nichol, C., Malthus, T., & Woodhouse, I. (2009). Assessing forest structural and physiological information content of multi-spectral lidar waveforms by radiative transfer modelling. *Remote Sensing of Environment*, *113*, 2152–2163.

Naesset, E. (2002). Predicting forest stand characteristics with airborne scanning laser using a practical two-stage procedure and field data. *Remote Sensing Of Environment*, *80*, 88–99.

Næsset, E. (2014). Area-Based Inventory in Norway – From Innovation to an Operational Reality. In M. Maltamo, E. Næsset, & J. Vauhkonen (Eds.), *Forestry Applications of Airborne Laser Scanning: Concepts and Case Studies. Managing Forest Ecosystems, 27* (pp. 215–240). Springer, The Netherlands. 464pp.

Nelson, R., Oderwald, R., & Gregoire, T. (1997). Separating the ground and airborne laser sampling phases to estimate tropical forest basal area, volume, and biomass. *Remote Sensing of Environment*, *60*, 311–326.

Ni-Meister, W., Jupp, D., & Dubayah, R. (2001). Modeling lidar waveforms in heterogeneous and discrete canopies. *IEEE Transactions on Geoscience and Remote Sensing*, *39*, 1943–1958.

Nilsson, M. (1996). Estimation of tree heights and stand volume using an airborne lidar system. *Remote Sensing of Environment*, *56*, 1–7.

Ørka, H., Næsset, E., & Bollandsås, O. (2009). Classifying species of individual trees by intensity and structure features derived from airborne laser scanner data. *Remote Sensing of Environment*, *113*, 1163–1174.

Oshiro, T., Perez, P., & Baranauskas, J. (2012). How many trees in a random forest? *Lecture Notes in Computer Science*, *7376 LNAI*, 154–168.

Pal, M., & Mather, P. M. (2006). Some issues in the classification of DAIS hyperspectral data. *International Journal Of Remote Sensing*, *27*, 2895–2916.

Persson, Å., Söderman, U., Töpel, J., & Ahlberg, S. (2005). Visualization and analysis of full-waveform airborne laser scanner data. *International Archives of Photogrammetry, Remote Sensing and Spatial Information Sciences*, *36*, 103–108.

R Development Core Team (2016). *R: A language and environment for statistical computing*. R Foundation for Statistical Computing, Vienna, Austria.

Reitberger, J., Krzystek, P., & Stilla, U. (2008). Analysis of full waveform LIDAR data for the classification of deciduous and coniferous trees. *International Journal Of Remote Sensing*, *29*, 1407–1431.

Richter, K., Blaskow, B., Stelling, N., & Maas, H.-G. (2015). Reference value provision schemes for attenuation correction of full-waveform airborne laser scanner data. *ISPRS Annals of Photogrammetry, Remote Sensing and Spatial Information Sciences. ISPRS Geospatial Week 2015, 28 September–3 October 2015, La Grande Motte, France*, (pp. 65–72).

RIEGL (2012). *LMS-Q680i, Datasheet*. RIEGL Laser Measurement Systems GmbH, Horn, Austria.

RIEGL (2013). Products. Software Packages. RiWaveLIB v1.5.241. RIEGL Laser Measurement Systems GmbH, Horn, Austria. Retrieved from: http://www.riegl.com/index.php?id=322 (17.3.2016).

RIEGL (2014). *Waveform Extraction Library, Datasheet*. RIEGL Laser Measurement Systems GmbH, Horn, Austria.

Romanczyk, P., van Aardt, J., Cawse-Nicholson, K., Kelbe, D., Mc, J., & Krause, K. (2013). Assessing the impact of broadleaf tree structure on airborne full-waveform small-footprint lidar signals through simulation. *Canadian Journal of Remote Sensing*, *39*, S60–S72.

Roncat, A. (2014). *Backscatter signal analysis of small-footprint full-waveform lidar data*. Ph.D. thesis Fakultät für Mathematik und Geoinformation, Department für Geodäsie und Geoinformation, TU Wien, Wien.

Roncat, A. (in review). Full-Waveform-Laserscanning: Moment(e), da geht noch mehr! *Österreichische Zeitschrift für Vermessung und Geoinformation*, *2*.

Roncat, A., Bergauer, G., & Pfeifer, N. (2011). B-spline deconvolution for differential target cross-section determination in full-waveform laser scanning data. *ISPRS Journal Of Photogrammetry And Remote Sensing*, *66*, 418–428.

Roncat, A., Wagner, W., Melzer, T., & Ullrich, A. (2008). Echo detection and localization in full-waveform airborne laser scanner data using the averaged square difference function estimator. *The Photogrammetric Journal of Finland*, *21*, 62–75.

Schaepman, M., Ustin, S., Plaza, A., Painter, T., Verrelst, J., & Liang, S. (2009). Earth system science related imaging spectroscopy-an assessment. *Remote Sensing of Environment*, *113*, S123–S137.

Schneider, F. D., Leiterer, R., Morsdorf, F., Gastellu-Etchegorry, J.-P., Lauret, N., Pfeifer, N., & Schaepman, M. E. (2014). Simulating imaging spectrometer data: 3D forest modeling based on LiDAR and in situ data. *Remote Sensing Of Environment*, *152*, 235–250.

Sun, G., & Ranson, K. (2000). Modeling lidar returns from forest canopies. *IEEE Transactions on Geoscience and Remote Sensing*, *38*, 2617–2626.

Torabzadeh, H., Morsdorf, F., Leiterer, R., & Schaepman, M. E. (2014). Fusing imaging spectrometry and airborne laser scanning data for tree species discrimination. In *2014 IEEE Internation Geoscience and Remote Sensing Symposium (IGARSS)* (pp. 1253–1256).

Torabzadeh, H., Morsdorf, F., & Schaepman, M. (2014). Fusion of imaging spectroscopy and airborne laser scanning data for characterization of forest ecosystems - a review. *ISPRS Journal of Photogrammetry and Remote Sensing*, *97*, 25–35.

Ustin, S., Roberts, D., Gamon, J., Asner, G., & Green, R. (2004). Using imaging spectroscopy to study ecosystem processes and properties. *BioScience*, *54*, 523–534.

Vaughn, N., Moskal, L., & Turnblom, E. (2012). Tree species detection accuracies using discrete point lidar and airborne waveform lidar. *Remote Sensing*, *4*, 377–403.

Vauhkonen, J., Maltamo, M., McRoberts, R. E., & Næsset, E. (2014). Introduction to Forestry Applications of Airborne Laser Scanning. In M. Maltamo, E. Næsset, & J. Vauhkonen (Eds.), *Forestry Applications of Airborne Laser Scanning: Concepts and Case Studies. Managing Forest Ecosystems, 27* (pp. 1–16). Springer, The Netherlands. 464pp.

Wagner, W. (2010). Radiometric calibration of small-footprint full-waveform airborne laser scanner measurements: Basic physical concepts. *ISPRS Journal Of Photogrammetry And Remote Sensing*, *65*, 505–513.

Wagner, W., Hollaus, M., Briese, C., & Ducic, V. (2008a). 3d vegetation mapping using small-footprint full-waveform airborne laser scanners. *International Journal of Remote Sensing*, *29*, 1433–1452.

Wagner, W., Hyyppä, J., Ullrich, A., Lehner, H., Briese, C., & Kaasalainen, S. (2008b). Radiometric calibration of full-waveform small-footprint airborne laser scanners. *International Archives of Photogrammetry, Remote Sensing and Spatial Information Sciences*, *38 (Part B1)*, 163–168.

Wagner, W., Ullrich, A., Ducic, V., Melzer, T., & Studnicka, N. (2006). Gaussian decomposition and calibration of a novel small-footprint full-waveform digitising airborne laser scanner. *ISPRS Journal Of Photogrammetry And Remote Sensing*, *60*, 100–112.

Wagner, W., Ullrich, A., Melzer, T., Briese, C., & Kraus, K. (2004). From single-pulse to full-waveform airborne laser scanners: potential and practical challenges (Part B3). In *International Archives of the Photogrammetry, Remote Sensing and Spatial Information Sciences 35* (pp. 201–206). Istanbul, Turkey.

Wolfram (2016). Wolfram Language and Systems, Documentation Center, NakagamiDistribution. Retrieved from: https://reference.wolfram.com/language/ref/NakagamiDistribution.html (16.1.2016).

Wulder, M., Bater, C., Coops, N., Hilker, T., & White, J. (2008). The role of lidar in sustainable forest management. *Forestry Chronicle*, *84*, 807–826.

Wulder, M., Coops, N., Hudak, A., Morsdorf, F., Nelson, R., Newnham, G., & Vastaranta, M. (2013). Status and prospects for lidar remote sensing of forested ecosystems. *Canadian Journal of Remote Sensing*, *39*, S1–S5.

Yu, X., Litkey, P., Hyyppä, J., Holopainen, M., & Vastaranta, M. (2014). Assessment of low density full-waveform airborne laser scanning for individual tree detection and tree species classification. *Forests*, *5*, 1011–1031.

Acknowledgements

First, I would like to thank my supervisor Felix for his continuous support, for providing me with many inputs, for his encouragement in times of doubt and for stopping me, when the approach seemed unpromising. Special thanks go to Andreas Roncat, who co-authored the article, for his time discussing the sensor specific issues. Likewise, I would like to thank Michael E. Schaepman.

I enjoyed the time at the RSL and would like to express my acknowledgements to the entire group. From those directly involved in my thesis, I would like to thank Reik Leiterer for providing me with relevant papers; Philip Jörg again for discussions concerning aspects of waveform decomposition and ALS data in general; Diego Marcos Gonzalez for his help in setting up the parallel computation pipeline; and Devis Tuia and Michele Volpi for their help regarding the classification framework. Furthermore, I would like to express my thanks to Carla Guillén Escribà for the improved tree species map; Fabian Daniel Schneider for the template of the thesis and his many inputs regarding efficient programming; Daniel Kükenbrink and Jonas Böhler for their tricks in MATLAB and Bruno Weber for the IT support.

I thank Stephan Landtwing for his insights into operational aspects of ALS data. Moreover I would like to thank Wolfgang Wagner and the Department of Geodesy and Geoinformation from TU Vienna for their invitation to Vienna and the possibility to present my results. The discussion after the presentation helped me define the further direction of the thesis.

Last but not least, I would like to thank my friends and family for support and understanding and my colleagues Dominic, Marius, Basil, Fiona, Nicholas and Kathy for the good time we’ve spent in the ”cave”, at bQm, in Scotland and in Wales. Cheers, lads!

A | Separability of tree species

Tab. A.1 shows the enhancement of Tab. 2.6 and additionally reports which tree species show significant differences on a $p = 0.05$ significance level. The thesis concentrated mainly on the evaluation of echo attributes regarding the differentiation power for tree species. This table shifts the perspective to the differences between the species. One can expect species with few differences in the attributes against each other to be similar regarding the interaction processes of the laser with the crowns.

Fig. A.1 and Fig. A.2 show the crown-wise aggregated attribute ranges for the mean aggregates per species, illustrating the differences reported in Tab. A.1. An excerpt of these plots was used in Fig. 2.6 where for each mean aggregated attribute, the echo type revealing the strongest differentiation power is depicted. The crown-wise standard deviation aggregates are depicted in Fig. A.3 and Fig. A.4.

Table A.1.: Summary of the ANOVA test for significant differences between species pairs for each echo attribute and echo type, distinguished in regard to the aggregation metrics on crown level. The evaluation is done on a $p = 0.05$ significance level, the number of trees is $N = 969$. For seven species, the maximum number of 21 combinations (pairs) are possible, which could theoretically be separated per attribute.

attribute	number of differences between species		differentiable species pairs	
	mean	*std. dev.*	*mean*	*std. dev.*
all_A_canopy	8	8	11-14, 14-22, 14-23, 14-29, 14-56, 23-31, 29-31, 29-56	11-14, 11-31, 14-23, 14-29, 22-31, 23-31, 29-31, 31-56
all_E_canopy	9	12	11-14, 11-29, 14-22, 14-23, 14-29, 14-31, 14-56, 29-31, 29-56	11-14, 11-23, 11-29, 14-22, 14-23, 14-29, 14-31, 14-56, 22-31, 23-31, 29-31, 29-56
all_fwhm_canopy	10	0	11-22, 11-23, 11-29, 11-31, 11-56, 14-22, 14-23, 14-29, 14-31, 14-56	-
all_skew_canopy	14	6	11-22, 11-23, 11-29, 11-31, 11-56, 14-22, 14-23, 14-29, 14-31, 14-56, 22-31, 22-56, 29-31, 29-56	11-29, 14-31, 22-31, 23-29, 29-31, 31-56
all_kurt_canopy	7	8	11-31, 14-23, 14-29, 14-31, 23-29, 29-31, 31-56	11-22, 11-29, 11-56, 22-23, 22-31, 23-29, 29-31, 31-56
first_A_canopy	14	9	11-14, 11-22, 11-23, 11-29, 14-22, 14-23, 14-29, 14-31, 14-56, 22-31, 23-31, 23-56, 29-31, 29-56	11-22, 11-29, 11-31, 14-29, 14-31, 23-29, 23-31, 29-56, 31-56
first_E_canopy	15	7	11-14, 11-22, 11-23, 11-29, 11-31, 11-56, 14-22, 14-23, 14-29, 14-31, 14-56, 23-31, 23-56, 29-31, 29-56	11-23, 14-23, 14-56, 23-29, 23-31, 29-56, 31-56
first_fwhm_canopy	11	12	11-14, 11-22, 11-23, 11-29, 11-31, 11-56, 14-31, 22-31, 23-31, 29-31, 31-56	11-22, 11-29, 14-22, 14-23, 14-29, 14-56, 22-31, 23-29, 23-31, 29-31, 29-56, 31-56
first_skew_canopy	7	8	11-22, 11-29, 11-56, 22-31, 23-29, 29-31, 31-56	11-22, 11-29, 14-29, 22-23, 22-31, 23-29, 29-31, 29-56
first_kurt_canopy	7	8	11-22, 11-29, 14-29, 22-31, 23-29, 29-31, 29-56	11-22, 11-29, 14-29, 22-23, 22-31, 23-29, 29-31, 29-56

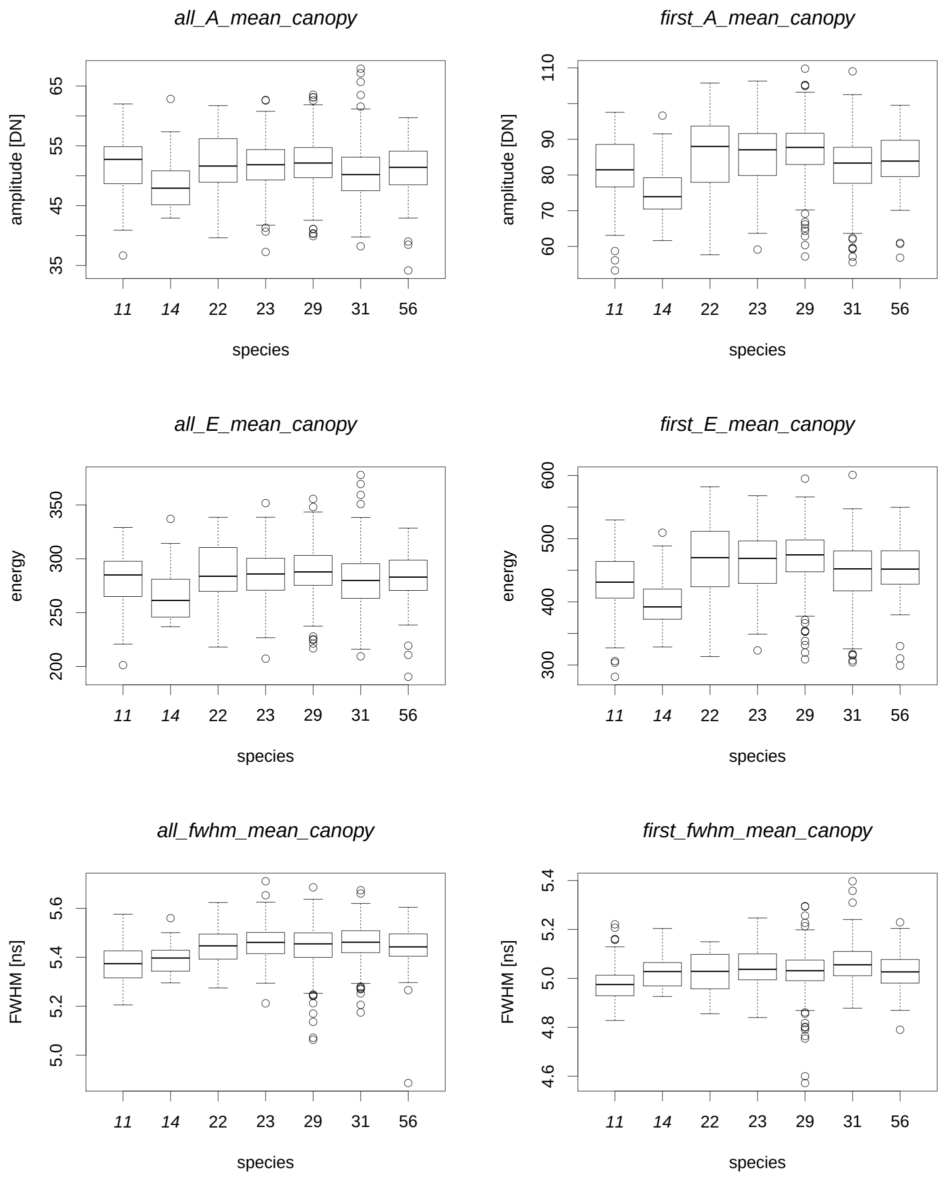
all_A_mean_canopy

first_A_mean_canopy

all_E_mean_canopy

first_E_mean_canopy

all_fwhm_mean_canopy

first_fwhm_mean_canopy

Figure A.1.: Differences across the species in the amplitude, energy and FWHM attributes. Depicted are the mean aggregates on crown level for the *all*-echoes (left) and for the *first*-echoes (right), respectively. Coniferous tree species are written in italic letters.

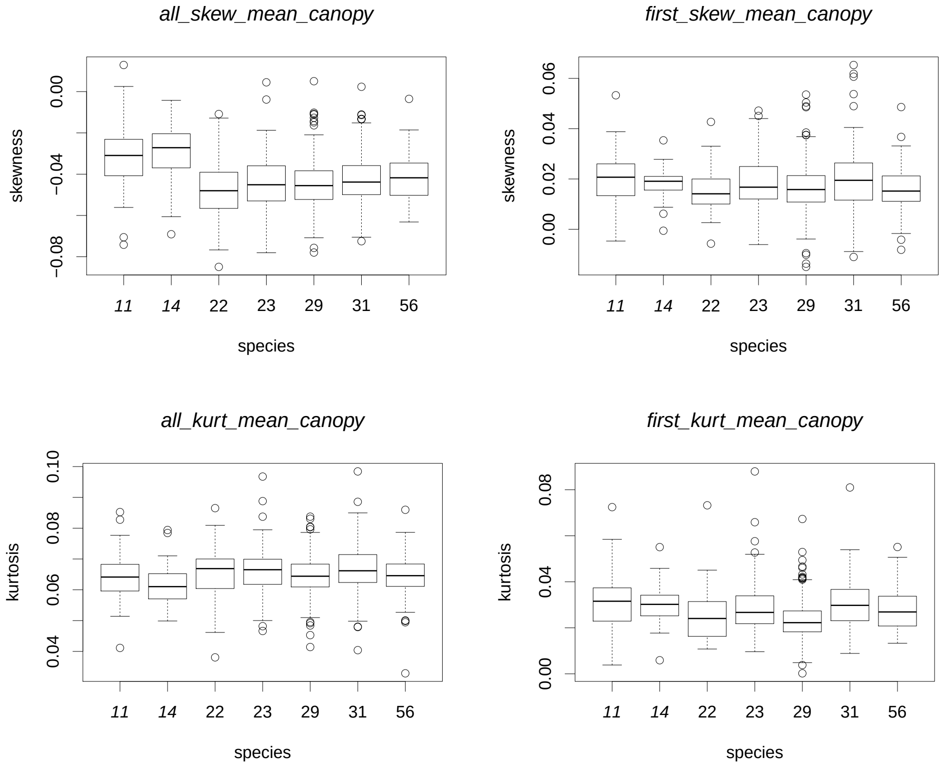

Figure A.2.: Differences across the species in the skewness and the kurtosis attributes. Depicted are the mean aggregates on crown level for the *all*-echoes (left) and for the *first*-echoes (right), respectively. The measure of the kurtosis is relative to the Gaussian distribution. Coniferous tree species are written in italic letters.

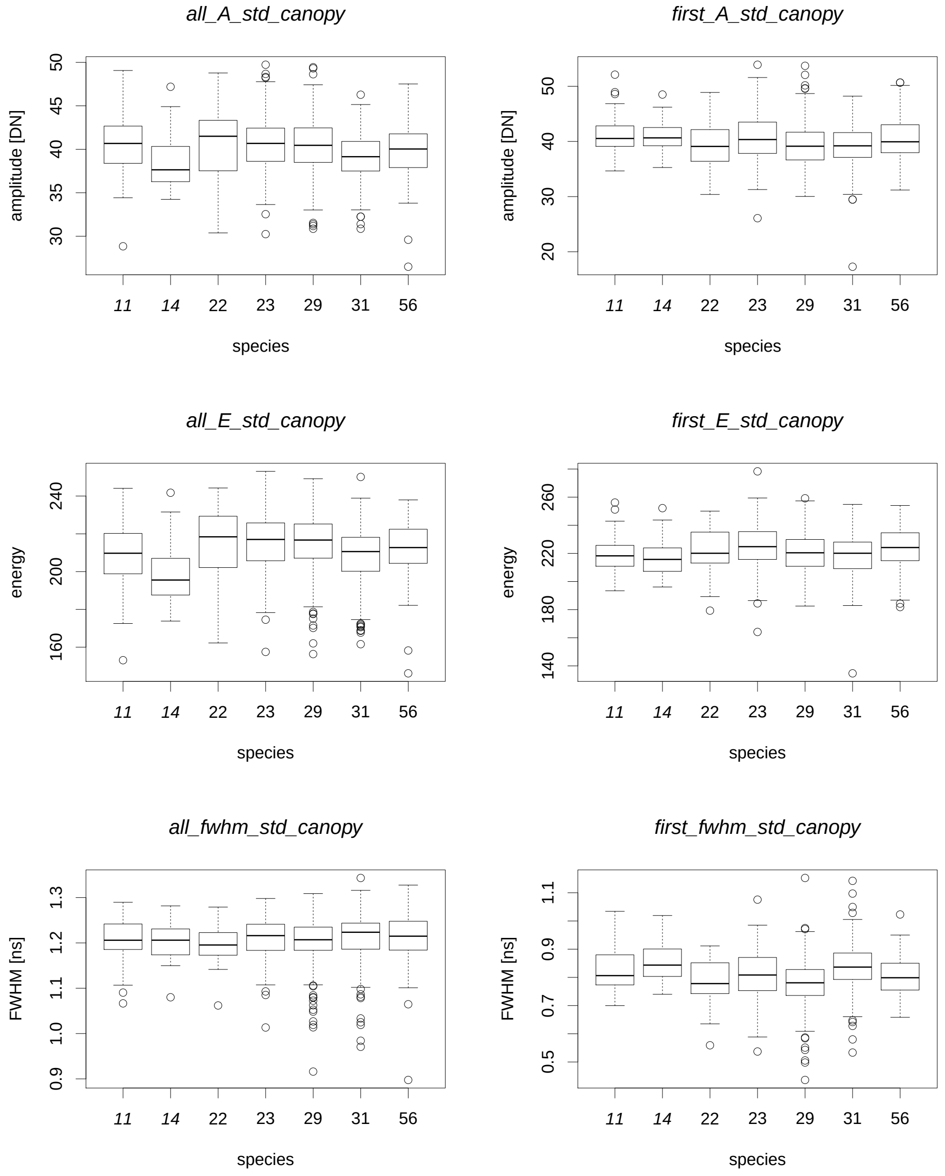

Figure A.3.: Differences across the species in the amplitude, energy and FWHM attributes. Depicted are the standard deviation aggregates on crown level for the *all*-echoes (left) and for the *first*-echoes (right), respectively. Coniferous tree species are written in italic letters.

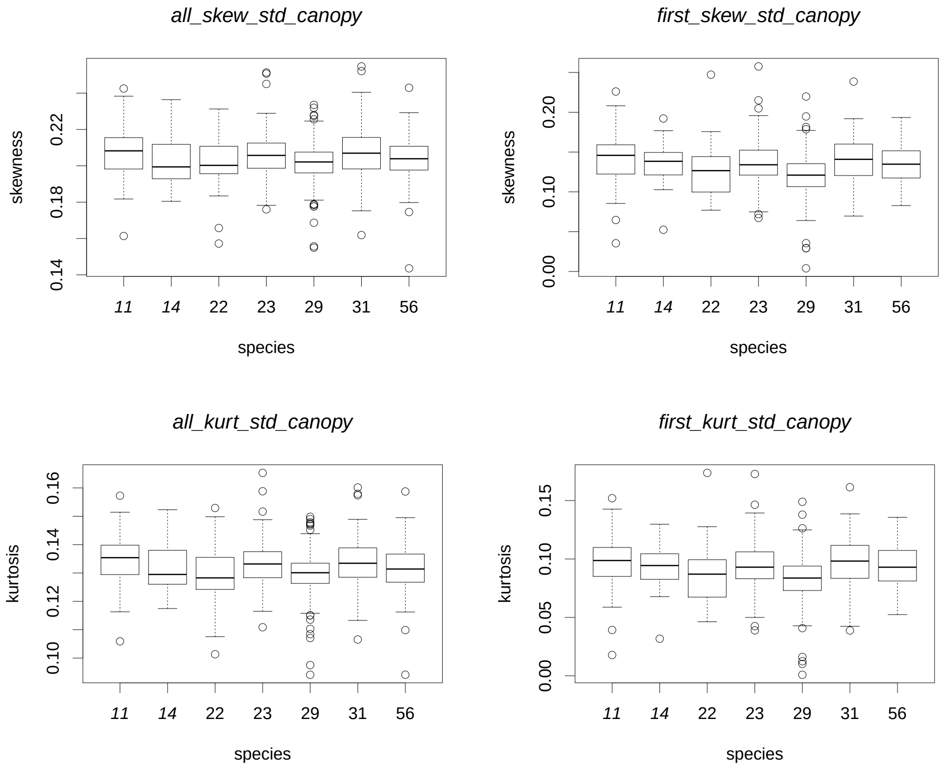

Figure A.4.: Differences across the species in the skewness and the kurtosis attributes. Depicted are the standard deviation aggregates on crown level for the *all*-echoes (left) and for the *first*-echoes (right), respectively. Coniferous tree species are written in italic letters.

Personal Declaration

I hereby declare that the submitted thesis is the result of my own, independent work. All external sources are explicitly acknowledged in the thesis.

Place, Date Signature